Simulating AGN Feedback by Line-driven Winds in Idealized Disc Galaxies

JINNING LIANG

How to cite:

LIANG, JINNING (2025) Simulating AGN Feedback by Line-driven Winds in Idealized Disc Galaxies. Masters thesis, Durham University.

Simulating AGN Feedback by Line-driven Winds in Idealized Disc Galaxies

Master's Thesis

Jinning Liang

`jinning.liang@durham.ac.uk`

Institute for Computational Cosmology
Department of Physics
Durham University

Supervisors:
Prof. Cedric Lacey
Dr. Sownak Bose

December 17, 2024

Declaration

I declare that this thesis has been composed solely by myself and that it has not been submitted, in whole or in part, in any previous application for a degree. Except where states otherwise by reference or acknowledgement, the work presented is entirely my own.

Statement of Copyright

Acknowledgements

I sincerely appreciate all supports and love that I receive during the time that I spent in Durham.

To begin with, I would like to express my deepest gratitude to my supervisor, Prof. Cedric Lacey, for his invaluable guidance. His profound knowledge of galaxies, black holes, and cosmology, combined with his boundless enthusiasm for astronomy, has been a constant source of inspiration. I am especially grateful for his unwavering kindness and support, particularly during challenging times in both my personal life and research. He was always thoughtful and considerate when I faced difficulties, struggling with my live. This work would not have been possible without him, and my time in Durham would not have been as smooth and fulfilling without his presence.

Secondly, I would like to sincerely thank my supervisor, Dr. Sownak Bose, and my senior and friend, Dr. Filip Huško, for their invaluable feedback during group discussions and their generous assistance with technical aspects of my research. Their expertise in cosmological simulations, combined with their support, helped me overcome many challenges efficiently. Thanks to their guidance, I was able to save valuable time and focus more deeply on the scientific aspects of my work.

I would like to thank Dr. Alastair Basden for his technical support of COSMA in time. I would also like to thank Durham Astronomy community including ICC and CEA, for their support throughout postgraduate life, providing handful opportunity to discuss with astronomer all over the world during countless seminar and colloquium. It is their efficient work enhanced my living experience in the OCW.

I would like to thank my roommates and friends including George, Tom, Weiting, Betty, Angel, Ashely, Dr. Zefeng Li and Lingyi Cheng, for your accompanies and the happiness that you brought to me. You made me feel at home, even though I was 9,000 kilometers away from my family.

I would like to thank my girlfriend Huanyan Wei and my parents for their remote support from China and I am sorry to let you suffer this.

Finally, I would like to acknowledge myself, who dedicate nearly all the time for pursuing his dream.

Abstract

Active Galactic Nuclei (AGN) feedback plays a crucial role in galaxy formation and evolution. AGN-driven winds, with large kinetic luminosities found observationally, could significantly impact the galaxies hosting the AGN. Radiation pressure on UV absorption lines is a promising mechanism for driving these winds, whose feedback effect remains to be explored.

In this thesis, I explore how AGN feedback influences the galaxy properties using a state-of-the-art cosmological hydrodynamical code – `SWIFT` with COLIBRE subgrid physics. I implement a new subgrid model for AGN feedback that couples feedback efficiency with the Eddington ratio by a power-law, based on scaling relations for line-driven winds from the analytical model Qwind. I simulated idelized Milky Way-like galaxies incorporating a black hole (BH), cold gas disc, stellar disc, and hot circumgalactic medium (CGMs) within a static dark matter halo potential. The black hole is assumed to accrete gas at the Bondi rate. I explore the effects of varying BH masses, the slope and the normalization in new coupling efficiency model.

I find that higher BH masses result in greater cumulative AGN energy injection, higher AGN energy injection rates, which in turn lead to lower star formation rates (SFR) and cold gas masses but higher gas outflow rates. When comparing fiducial variable coupling efficiency model with default constant coupling efficiency model, the former one produces weaker AGN feedback, characterized by reduced cumulative AGN energy injection, lower AGN energy injection rates, and significantly smaller coupling efficiencies, but higher accretion rates. This results in faster BH growth, larger SFR and cold gas masses, and lower gas outflow rates, while enhancing BH self-regulation. These effects are due to the coupling effeciency typically being lower in the variable efficiency model. Compared to some previous simulations, our results exhibit weaker AGN feedback and less suppression of SFR.

Contents

List of Tables

List of Figures

Chapter 1

Introduction

Active galactic nucleus (AGN) feedback from supermassive black holes (SMBH) residing at the centres of host galaxies are widely thought to be having large effects on galaxy formation and evolution, especially in the regulating growth of massive galaxies, by releasing significant amounts of energy into their surrounding gas (Kormendy & Ho, 2013; Fabian, 2012). While other feedback processes including stellar feedback can account for the suppression of star formation in dwarf galaxies, they cannot explain the quenching of massive galaxies. Implementation of AGN feedback helps us to address the gap, successfully suppress star formation in massive galaxies (Harrison, 2017). However, while current models accounting for AGN feedback can reproduce key observational relations, such as the stellar mass function and the stellar mass–black hole mass relation, their success is based on simplified, phenomenological prescriptions for AGN feedback, with adjustable parameters that are tuned to reproduce the above observations (Schaye et al., 2015; Pillepich et al., 2018). Discrepancy might be shown when comparing some properties that are not used to do calibration (e.g. quenching fraction that potentially related to AGN feedback, Donnari et al., 2021) These discrepancies suggest that our treatment of AGN feedback remains incomplete, potentially due to missing feedback modes or gaps in understanding the underlying physical mechanisms. Consequently, accurately modeling of AGN feedback as well as SMBH growth and dynamics has become essential in both observations and simulations and worthy to be investigated.

Black holes (BH) grow either by accreting surrounding materials (mainly gas) or by mergers with other BHs. Due to non-zero angular momentum of accreted materials, an accretion disc is generally formed around BHs (Volonteri, 2010). The nature of this disc, however, depends on the accretion rate normalized by Eddington rate. Clearly, understanding the type of accretion discs and their models are essential when studying AGN feedback (Shakura & Sunyaev, 1973; Narayan & Yi, 1994; Wang & Zhou, 1999). The following sections contain the introductions of accretion discs and basics of black hole accretion physics.

1.1 Accretion discs

1.1.1 Basics of accretion physics

To study accretion physics, one needs to know basic BH properties. For given BH mass $M_{\rm BH}$, radius R, the size of BH, i.e. the gravitational radius, can be characterized by

$$R_{\rm g} = \frac{GM_{\rm BH}}{c^2} \tag{1.1}$$

where G is gravitational constant and c is speed of light. Note that typical BH mass is $10^8 M_\odot$, corresponding to a size of 1.48×10^{13}cm or 4.8×10^{-6}pc.

The magnitude of the black hole's physical angular momentum is defined as

$$J = \frac{GM^2}{c} a \tag{1.2}$$

where a is the dimensionless black hole spin. The innermost stable circular orbit (ISCO) is given by $R_{\rm ISCO} = r_{\rm ISCO} R_{\rm g}$ and $r_{\rm ISCO}$ depends on spin.

The bolometric luminosity $L_{\rm bol}$ of a BH is related to its mass accretion rate $\dot{M}$ by

$$L_{\rm bol} = \epsilon_{\rm r} \dot{M} c^2 \tag{1.3}$$

where for thin accretion disc, $\epsilon_{\rm r} = 1 - \sqrt{1 - 2/(3r_{\rm ISCO})}$ is accretion radiative efficiency of 0.057, if assuming spin is 0. The radiation force for scattering on free electrons only, assuming pure ionized hydrogen gas, in spherical situation due to this luminosity is

$$F_{\rm rad} = \frac{L_{\rm bol}\sigma_{\rm T}}{4\pi c r^2} \tag{1.4}$$

where $\sigma_{\rm T} \simeq 6.65 \times 10^{-25}{\rm cm}^2$ is the Thomson cross-section. While radiation force push electrons and protons outward, they are also accreted by gravitational force

$$F_{\rm grav} \simeq \frac{G(m_{\rm p} + m_{\rm e})M_{\rm BH}}{r^2} \simeq \frac{GM_{\rm BH}m_{\rm p}}{r^2} \tag{1.5}$$

I define Eddington limit as $F_{\rm rad} = F_{\rm grav}$

$$L_{\rm Edd} = \frac{4\pi G M_{\rm BH} c}{\kappa} \simeq 1.3 \times 10^{46} M_8 \text{ erg s}^{-1} \tag{1.6}$$

where $\kappa \simeq \sigma_{\rm T}/m_{\rm p} \simeq 0.34{\rm cm}^2{\rm g}^{-1}$ is the electron scattering opacity and $M_8 = M/10^8 M_\odot$. The mass accretion rate with this limit is

$$\dot{M}_{\rm Edd} = \frac{L_{\rm Edd}}{\epsilon_{\rm r} c^2} = \frac{4\pi G M_{\rm BH}}{\epsilon_{\rm r} \kappa c} \tag{1.7}$$

The ratio between $M_{\rm BH}$ and $\dot{M}_{\rm Edd}$ is called Eddington ratio $\dot{m} = M_{\rm BH}/\dot{M}_{\rm Edd}$. Note the fact that not every particle in the gas contributes equally to the radiation pressure. In that case, one needs to multiply $L_{\rm Edd}$ by a factor of μ_e. This factor accounts for composition different from pure hydrogen. In a fully ionized hydrogen plasma, every proton contributes one free electron, which means that $\mu_e = 1$. However, in a plasma with heavier elements, fewer free electrons are available per baryon, increasing μ_e.

1.1.2 Types of accretion disc

Accretion disc models can be classified into three categories based on their geometry and $\dot{m}$: thin disc (α-disc, $0.01 - 0.03 \lesssim \dot{m} \lesssim 1$, Shakura & Sunyaev, 1973), thick disc ($\dot{m} \lesssim 0.01 - 0.03$, Narayan & Yi, 1994) and slim disc ($\dot{m} \gtrsim 1$, Abramowicz et al., 1988; Wang & Zhou, 1999). Note that the real accretion discs might be more complicated and involve combinations of these models, but they remain useful frameworks due to their simplicity and widespread use in studies. For example, some models of the UV line driven wind used to explain some ultrafast outflows (UFOs) that I will introduce below are still based on standard thin disc model but providing very useful insights (Quera-Bofarull et al., 2023).

The thin disc solution is firstly proposed by Shakura & Sunyaev (1973) and later Novikov & Thorne (1973) for its general-relativistic form. It describes a geometrically thin (with negligible thickness compared to its radius), optically thick (emitting blackbody-like radiation) and steady (constant accretion rate) accretion disc where interactions between gas layers through viscous torques cause gas inflow whilst maintaining almost Keplerian orbits. As a result, about 10 per cent of the total mass-energy of the matter in thin disc is radiated as observed in quasars (Yu & Tremaine, 2002; Davis & Laor, 2011). Thin disc is appearing at intermediate accretion rates ($0.01-0.03 \lesssim \dot{m} \lesssim 1$) with strong radiative efficiency but low jet efficiency.

When the accretion rate becomes super low ($\dot{m} \lesssim 0.01 - 0.03$), the accretion disc will be transitioned to a geometrically thick and optically thin disc, i.e. advection-dominated accretion flow (ADAF), proposed by Narayan & Yi (1994). The gas motion is dominated by advection with energy releasing from the thick disc close to the BH by very powerful relativistic jets (Blandford & Znajek, 1977) but weak and inefficient radiative feedback. Additionally, advection of magnetic field is also thought to play an important role (Spruit & Uzdensky, 2005). Therefore, previous work typically use GRMHD simulations to model BH spin, relativistic jets and magnetic field to study thick disc (McKinney et al., 2012).

The final regime occurs at super-Eddington accretion rate ($\dot{m} > 1$), where the disc exhibits properties from both previous models (Wang & Zhou, 1999). It is optically thick, geometrically thick and advection dominated with both strong jets if the BH is spinning (McKinney et al., 2014) and strong radiation pressure dominant over gas pressure (Jiang et al., 2014). Although it is rarely used to explain local observed AGN, some studies suggest that it might be applicable to high redshift ultraluminous AGN (Gladstone et al., 2009; Jiang et al., 2014).

1.2 AGN feedback

Once different types of accretion discs are formed, they inject significant amounts of energy into the surrounding gas, influencing their host galaxies through a process known as AGN feedback. This feedback occurs in two main types: "wind feedback" and "jet feedback". Winds are thought to be launched from accretion disc mainly due to a combination of radiation pressure on dust, thermal pressure, and magnetic forces, as observed in some luminous AGN (King & Pounds, 2015). These winds are generally isotropic or partly collimated and exhibiting lower speeds and maybe lower energy outputs compared to jets, although some UFO suggest that winds can be strongly collimated (less than jets, Tombesi et al., 2010a). This will be discussed below. In contrast, jets are highly collimated, and relativistic, delivering significant kinetic energy to the gas and push them into circumgalactic or intracluster medium scale, as observed directly through radio and X-ray observations of the central galaxies of cool core clusters (McNamara et al., 2005; McNamara & Nulsen, 2007). The detailed driving mechanism and connection between these two feedback types haven't been fully confirmed. But from observations, these two feedback mechanisms are not completely independent, and an SMBH may switch between them depending on accretion rateand galaxy properties (Fabian, 2012).

As a consequence of AGN feedback, large-scale galactic outflows might be driven. These outflows are thought to typically involve fast winds from the accretion disk interacting with the interstellar medium (ISM), creating an inner reverse shock that slows the wind and an outer forward shock that accelerates the swept-up gas. These outflows can be further categorized into "momentum conserving" outflow or "energy conserving" outflow. For "momentum conserving" outflow, the shocks are rapidly cool to become effectively isothermal, which making them very narrow, while only the ram pressure is interacting to the outflow (King, 2003, 2005). Here, energy is not conserved since most of the energy released by the interaction of the AGN-driven wind with the ISM is radiated away. But the momentum from ram pressure is conserved. Consequently, the impact on the ambient medium is relatively localized and less energetic, resulting in a slower expansion of the swept-up gas shell. For "energy conserving" outflow, cooling in the shocked region is inefficient, leading to energy conserved, and the shocked regions are much wider (King, 2005; King et al., 2011). This allows both the thermal pressure and ram pressure to contribute to driving the outflow. Since energy is approximately conserved, the outflow injects a significant amount of heat into the swept-up gas shell, which can drive a more substantial and faster expansion of the swept-up gas shell. This creates a larger and more dynamically impactful influence on the ambient medium, potentially clearing larger volumes of gas from the galaxy.

Although both wind feedback and jet feedback are thought to play vital important roles in regulating galaxy growth (Kormendy & Ho, 2013; Fabian, 2012), the details of how AGN feedback operates remain debated (Harrison & Ramos Almeida, 2024). The feedback may potentially be either negative (suppress star formation, Di Matteo et al., 2005; Sijacki & Springel, 2006; Bower et al., 2006; Hopkins et al., 2008; Booth & Schaye, 2009) or positive (trigger star formation, Silk, 2005, 2013; Zubovas et al., 2013; Ishibashi et al., 2013), potentially depending on whether outflow is "energy conserving" or "momentum conserving" described above (Zubovas & King, 2012; Costa et al., 2014; Silk et al., 2024), as well as the time scale involved after the AGN feedback event. Initially, momentum-conserving outflows might dominate, creating turbulence that promotes star formation, while "energy conserving" outflow will take over as cooling becomes ineffective over time, and when the shocks move further from AGN (King, 2005; King et al., 2011; Silk et al., 2024). The shocks generated by "energy conserving" outflow expand adiabatically and expel the gas by releasing energy of the wind to the outflow, depleting the gas reservoir and suppressing star formation. Note that such explanation including the effect and the happening time, is from some models, which haven't fully proved to be true.

Given uncertainties above in AGN feedback, and the importance of AGN feedback to galaxy formation and evolution, numerous researches has been conducted over the past two decades. In recent researches, the AGN feedback and accretion disc modeling have been explored in cosmological hydrodynamical simulations, simulations of BHs and their accretion discs, and analytical or semi-analytical models, although they are still simple. Each approach offers different insights but also faces limitations. In some cosmological simulations, e.g. EAGLE, AGN wind feedback is simply implemented as the deposition of thermal energy into the surrounding gas isotropically, representing wind feedback. This is because most cosmological simulations lack enough resolution to distinguish radiative thermal feedback and kinetic feedback but this method is physically reasonable since the kinetic energy released by winds can eventually present as thermal energy by thermalizing and interacting with gas through shocks and turbulence. Then rapid gas cooling can be prevented and furthermore star formation suppressed. While this model is simplified, it can lead to excellent agreement with both optical and detailed X-ray observations of groups and clusters (McCarthy et al., 2010, 2011; Le Brun et al., 2014). Such simulations include Magneticum (Hirschmann et al., 2014), EAGLE (Schaye et al., 2015) and ASTRID (Bird et al., 2022). Other simulations, such as Illustris (Vogelsberger et al., 2014), IllustrisTNG (Springel et al., 2018; Marinacci et al., 2018; Nelson et al., 2018; Pillepich et al., 2018; Springel et al., 2018), SIMBA (Davé et al., 2019), Horizon-AGN (Kaviraj et al., 2017) and New-Horizon (Dubois et al., 2021), also consider kinetic feedback, with a transition dependent on accretion rate and BH mass. Specially, SIMBA, Horizon-AGN and New-Horizon employ a bipolar kinetic jet feedback while Illustris and IllustrisTNG use thermal hot bubble and kinetic isotropic feedback to represent the effect of kinetic jets, respectively (Sijacki et al., 2015; Weinberger et al., 2018).

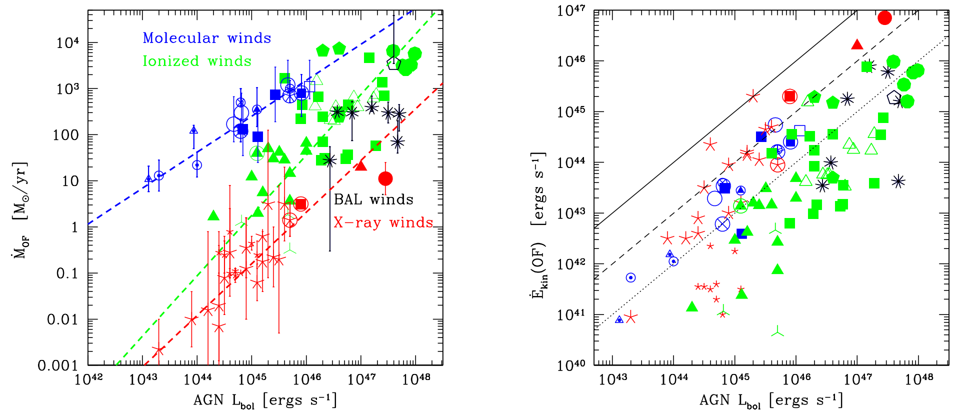

Figure 1.1: The wind mass outflow rate (left panel) and wind energy outflow rate (right panel) as a function of the AGN bolometric luminosity. Molecular winds, ionized winds, BAL winds and X-ray winds are represented by blue, green, black and red, respectively while different markers represent different observations. The dashed lines in the left panel are their best fit relations. Solid, dashed and dotted line in the right panel represent the correlations $\dot{E}_{\mathrm{kin}}(\mathrm{OF}) = 1, 0.1, 0.01 L_{\mathrm{bol}}$. Figure is taken from Fiore et al. (2017).

While cosmological simulations offer valuable insights into galaxy evolution on large scales, their treatment of AGN feedback remains simplified due to resolution limitations as well as missing physics. In contrast, simulations of BHs and their accretion discs capture additional physics in accretion disc including general relativity, radiative transfer or magnetohydrodynamics (Narayan et al., 2012; Higginbottom et al., 2014; Nomura et al., 2016; Yuan et al., 2018; Jiang et al., 2019; Higginbottom et al., 2024). However, they lack the contribution from galaxies and their environments when studying evolution of BHs. Besides, expensive computation time is another problem.

AGN can also be simply modeled by galaxy semi-analytical models (Lacey et al., 2016; Henriques et al., 2020) which populate dark matter haloes from N-body simulations with galaxy properties obtained from empirical or theoretical relations. Similarly, in semi-empirical model (Behroozi et al., 2019; Zhang et al., 2023), they obtain BH properties by using empirical relations instead of direct modeling from AGN feedback. While they are less time-consuming than cosmological simulations, these models are constrained by current observations which can only capture limited properties of BHs and AGN feedback, similar to cosmological simulations. There are also some analytical and semi-analytical models for AGN only (Dittmann & Cantiello, 2024; Risaliti & Elvis, 2010; Quera-Bofarull et al., 2020, 2023). Although they are computational cheap compared to GRMHD, they can only consider a few cases of accretion disc with assumptions.

Consequently, a comprehensive understanding of AGN feedback requires bridging the gap between these different treatments, integrating the strengths of them while mitigating their limitations. To build more unified AGN framework in galaxy and cosmological content, some studies have attempted to implement detail AGN simulation or (semi-) analytical AGN and accretion disc models into idealized galaxy simulations or zoom-in cosmological simulations (Costa et al., 2020; Koudmani et al., 2024), which is one of motivations of this thesis.

In this thesis, I study feedback by AGN winds. Observationally, AGN winds are categorised into molecular winds, ionised winds, broad absorption line (BAL) winds and X-ray winds, which are connected by wind parameters, AGN properties and spatial scales (Fiore et al., 2017). Physically, X-ray and BAL winds observed at small galactic radii may well drive ionized and molecular winds observed at larger radii. All of them show strong correlation between AGN bolometric luminosity and AGN wind mass outflow rate, as can be seen in Fig. 1.1. At the same bolometric luminosity, molecular wind show highest wind mass outflow rate, while other winds lie below the correlation found for molecular winds. Higher differences with respect to molecular winds are shown at lower bolometric luminosities. But for kinetic energy outflow rate, similar values exhibited for X-ray and molecular winds, but BAL and ionized winds generally lower, at the same AGN bolometric luminosities. When comparing their maximum wind velocity, $v_{\max}$, and relate it with bolometric luminosity, strong correlations are also found for all winds, as shown in Fig. 1.2. X-ray winds can be divided into two groups in this diagram, warm absorbers with lower velocities and UFOs with higher velocities ($v_{\max} > 10^4$ km s^{-1}). Although, both of them show correlation between bolometric luminosity and $v_{\max}$, the warm absorber is more close to molecular winds, ionized winds and BAL, whose $v_{\max}$ is abut 100 times smaller compared to UFOs . When compare their wind momentum load in Fig. 1.2 (outflow mo-

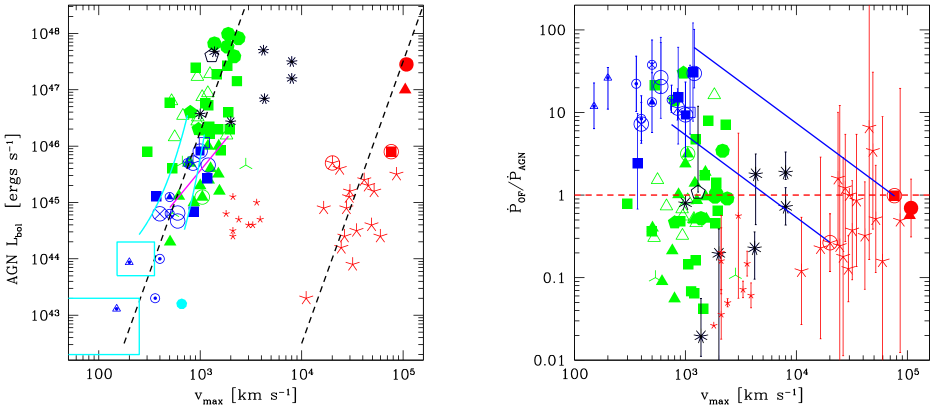

Figure 1.2: AGN bolometric luminosity (left panel) and wind momentum load (outflow momentum rate divided by the AGN radiation momentum rate $L_{\rm bol}/c$, right panel) as a function of the maximum wind velocity, $v_{\rm max}$. The black dahsed lines in the left panel mark a $v_{\rm max}^5$ scaling while magenta and cyan solid line represent best fit from other observations. In the right panel, the red dashed line mark the expectations for a momentum conserving outflow driven by radiation pressure with 100% efficiency of converting momentum of radiation from the AGN accretion disk into momentum of the outflow. The two blue solid lines mark the expectations for pure energy conserving outflows from other observations. The color scheme is the same as Fig. 1.1.

mentum rate divided by the AGN radiation momentum rate $L_{\rm bol}/c$), molecular winds are observed to have momentum load in the range 3–100, about half have momentum load >10, suggesting that such massive-extended outflows are energy conserving winds ($\dot{P}_{\rm OF}/\dot{P}_{\rm AGN} \approx v_{\rm UFO}/v_{\rm OF}$), extended on the host galaxy scales. For most BAL and X-ray winds, they have momentum load $\lesssim$1, suggesting that they could be radiation-driven outflow.

Specifically, the most powerful of these winds, i.e. highly ionized UFOs, exhibiting high velocities ($v \sim 0.1 - 0.3c$) and large kinetic luminosities ($L_{\rm kin} \sim 0.1\% - 10\% L_{\rm Edd}$ or $\sim 1\% - 50\% L_{\rm bol}$), is the most interesting wind and the motivation in this thesis. They are observed in 20–40% of local AGN (e.g. Tombesi et al. (2010b)) and in a handful of higher redshift objects (e.g. Chartas et al., 2009; Lanzuisi et al., 2012), made by highly ionised gas which can be detected only at X-ray energies, e.g. blueshifted Fe K-shell absorption lines in X-ray spectra of AGN (Tombesi et al., 2010a; Gofford et al., 2015), which likely originating from close to the accretion disc around SMBH. A promising mechanism to drive these UFOs is radiation pressure on UV absorption lines, where there are multiple strong atomic transitions in low ionization material (Proga et al., 2000). With absorb enough photon momentum, strong winds will be launching as similarly seen from O-star photospheres (Castor et al., 1975). Such large kinetic luminosities ($L_{\rm kin} \sim 0.1\% - 10\% L_{\rm Edd}$ or $\sim 1\% - 50\% L_{\rm bol}$) imply that these winds could have important feedback effects, e.g. remove significant amounts of gas from the host galaxies and regulate star formation. This kind of wind is called UV line driven wind. Some (semi-) analytical models and simulations of BHs and their accretion discs aim to model the launching of UV line driven winds (Nomura et al., 2016; Risaliti & Elvis, 2010; Higginbottom et al., 2014; Quera-Bofarull et al., 2020, 2023; Higginbottom et al., 2024) but no work attempts this into hydrodynamical cosmological code to study their influence on galaxy evolution in cosmological context. Therefore, in this thesis, our aim is to incorporate these predictions for line driven winds into a new model for AGN feedback in idealized galaxy evolution simulation, and investigate the effects on the evolution of galaxies and their SMBHs.

1.3 Thesis outline

In this thesis, I implement a new model for the coupling efficiency (the fraction of $L_{\rm bol}$ that can be transferred to AGN energy), which as a power law of Eddington ratio, into AGN feedback module of `SWIFT` code (Schaller et al., 2024) and simulate a series of isolated MW-like galaxies using COLIBRE subgrid physics model (Schaye et al, in prep.) to investigate the influence of this model on galaxy properties, i.e. star formation history, outflow rate, etc. I demonstrate that in Chapter 2, I briefly introduce the driving mechanism of line driven winds by using semi-analytical or simplified numerical model Qwind (Quera-Bofarull et al., 2023) and show how I motivated by scaling relations from Qwind. The `SWIFT` code and COLIBRE model will be illustrated in Chapter 3 where I also describe our implementation of new coupling efficiency model. I also list initial conditions (ICs) for all components of the simulations I have run and discuss how their parameters were chosen. Chapter 4 contains our analysis for our results whereas Chapter 5 contains our our conclusions and prospecting for future improvements.

CHAPTER 2

Line Driven winds

Observations show that UFOs are likely launched from accretion discs around SMBHs. These outflows typically exhibit high hydrogen column densities of approximately $N_{\mathrm{H}} \sim (10^{22} - 10^{24})\mathrm{cm}^{-2}$, moderate to high ionization parameters of approximately $\xi \sim (10^{3} - 10^{6})\mathrm{erg\ cm\ s}^{-1}$ (dominated by extremely highly ionized species including Fe XXV and Fe XXVI), and reach velocities of approximately $v \sim (0.1 - 0.3)c$ (King & Pounds, 2015). Such high outflow velocity result in large kinetic luminosity, which means that they are likely to have have important feedback effects on the host galaxies by injecting large energy into gas around SMBHs. UV line driving is one of promising mechanisms to explain UFOs, as the typical AGN accretion disc spectrum peaks in the UV range. It was firstly applied in O-star study by CAK formalism (Castor et al., 1975), and later extended to AGN studies, through analytical models (Murray et al., 1995; Risaliti & Elvis, 2010; Quera-Bofarull et al., 2020, 2023) and radiation hydrodynamic (RHD) simulations (Proga et al., 1998; Nomura et al., 2016; Higginbottom et al., 2014, 2024). However, RHD simulations are computationally expensive due to complicated radiative transfer processes, which require solving a network of equations at each timestep. In this chapter, I will introduce driving mechanism for UV line driven winds especially how to calculate radiation force, and use the analytical model Qwind to show scaling relations predicted by UV line driven winds. I will also explain how these scaling relations motivate the implementation of new AGN models in cosmological hydrodynamical codes, e.g. `SWIFT`.

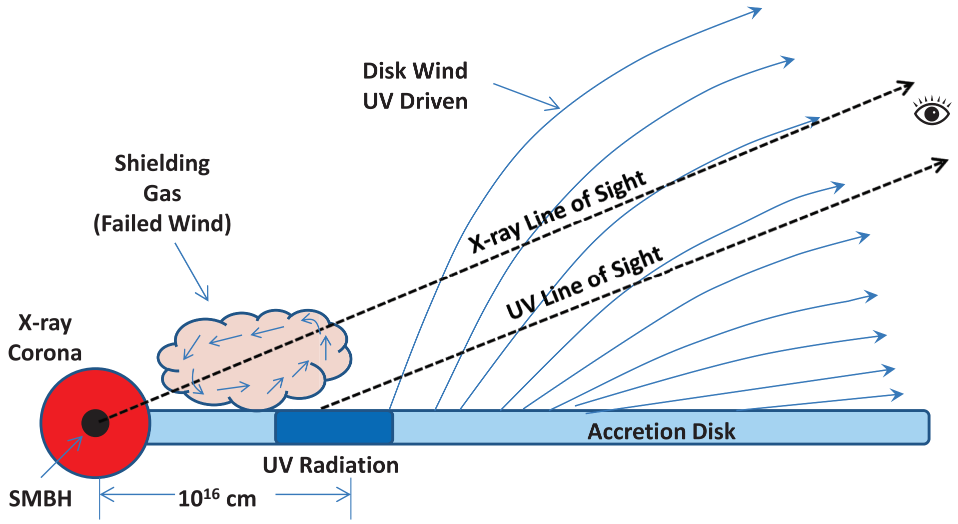

Figure 2.1: **A schematic diagram of the UV line driven wind scenario for UFOs.** The wind is launched from the accretion disc at $\sim 10^{16}$cm and is driven by UV radiation from the disc. The shielding gas, i.e. failed wind located at the base of the overionized wind blocks the X-ray radiation from the X-ray corona around SMBH and prevents the successfully launched wind from being overionized. Figure taken from Luo et al. (2013).

2.1 Driving mechanism

The reason why gas can be pushed outward from the SMBH scale to the galaxy scale is straightforward: the radial force generated by radiative pressure exceeds the radial gravitational force of the SMBH after the wind is launched[1]. The gravitational force can be easily calculated using Newton's law of gravitation, provided the gas is not too close to the SMBH. However, the calculation of outward forces varies across different models, depending on the source, e.g. thermal driving, radiative driving or magnetic driving, being considered when explaining AGN winds. In the case of UV line-driven winds, the outward force is from UV continuum, which will be discuss later. The radiation force can be divided into two components: X-ray and UV, as illustrated in Fig. 2.1. These components have contrasting effects: X-ray photons ionize the gas by interacting with accretion disc material via bound-free transitions with outer electrons, while UV opacity increases when the gas is not overly ionized, allowing UV photons to

---

[1] Here, I ignore hydrodynamic forces, as they are expected to be only comparable to gravity during the launching phase

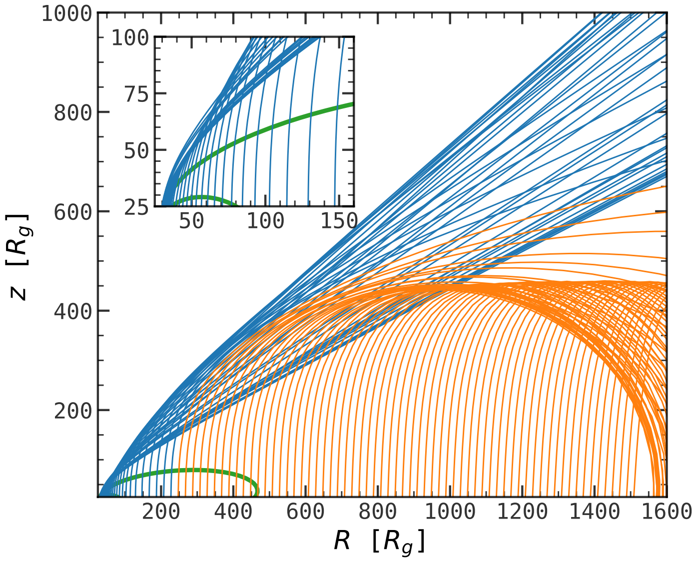

Figure 2.2: Results of a wind simulation, using Qwind code assuming $M_{\rm BH} = 10^6 M_\odot$ and $\dot{m} = 0.5$. The inner failed wind, escaping wind, and outer failed wind regions are coloured in green, blue, and orange, respectively. The inserted panel represent the same quantities but for the zoom-in regime from $R = 25R_{\rm g}$ to $R = 160R_{\rm g}$. The inner wind failed because strong ionization while outer wind failed because the amount of UV photons decreases significantly. **This figure visualizes inner failed wind, outer failed wind and escaping wind launched at different radii.**

excite electrons to higher energy states and transfer momentum to the gas.

If the gas is not too close to the X-ray corona, sufficient momentum from UV photons will be transferred to the gas, enabling it to reach the gravitational escape velocity and create an outflow. However, if the gas is too close to the X-ray corona, it becomes overionized, reducing the radiation force below the gravitational force. In this case, the gas will fall back to the disc as a failed wind, as shown in Fig. 2.1 and green lines shown in Fig. 2.2. The gas cannot be too far from the central region, as the amount of UV photons decreases significantly at larger radii, which can be seen in orange lines in Fig. 2.2. This process is known as UV line driving.

The mechanism that launches gas upward is similar: the vertical radiation force from the UV-emitting disk, countering both vertical gravitational and hydrodynamic forces. Here the hydrodynamic force is not ignorable and X-ray component in radiation force is very weak. Therefore, nearly all gas at different

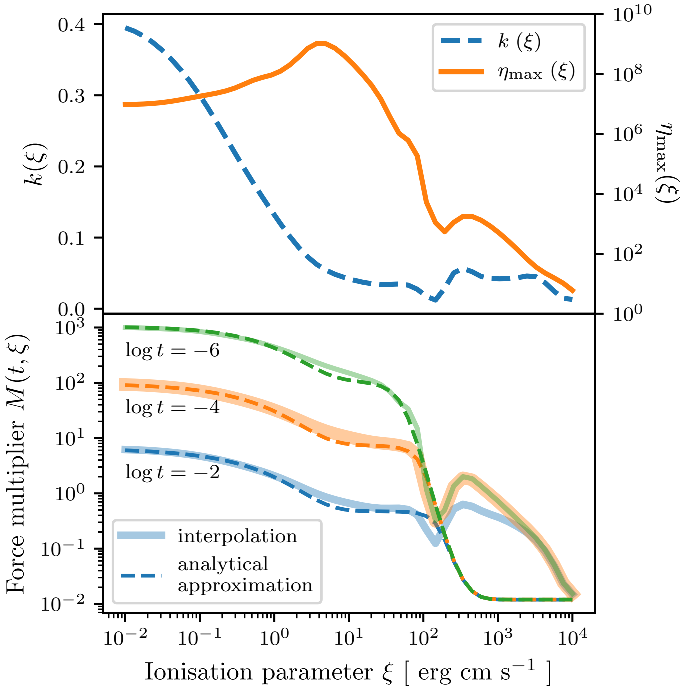

Figure 2.3: Upper panel: Best fit values for the force multiplier parameters k and $\eta_{\max}$ as a function of ionisation parameter ξ, from Stevens & Kallman (1990). Lower panel: force multiplier as a function of the ionisation parameter and the effective optical depth. Note that t in the figure refers to τ_{eff} in this thesis. Figure is taken from Quera-Bofarull et al. (2020). **This figure indicates how force multiplier and its component change with ionisation parameter, which is related to the radii of the wind.**

radii can be launched, although some of them will eventually fall back.

2.2 Simplified model - Qwind

In this section, I will further reveal the physical rationale of line-driven winds, particularly focusing on the radiation force, using the Qwind model. I will show some results by running Qwind with different black hole properties. Qwind is an simplified and non-hydrodynamical model originally developed by Risaliti & Elvis (2010), and further developed in Quera-Bofarull et al. (2020) and Quera-Bofarull et al. (2023). The core idea is that Qwind calculated the ballistic trajectories of gas blobs launched from an accretion disc and illuminated by both UV and X-ray flux. It neglects the contribution of hydrodynamical force except in the launching phase, making the code computationally much cheaper than full hydrodynamical simulation with radiative transfer and allowing for quick exploration of wind properties across a wide parameter space. In the next subsection, I will explain how radiation forces are calculated in Qwind, and demonstrate how both X-ray and UV flux contribute to these forces to drive the winds.

2.2.1 Radiation force

The radiation force can be decomposed into an X-ray component and a UV component as discussed previously. From CAK formalism (Castor et al., 1975), the total radiation force is amplified by line opacity, i.e. $\kappa_{\text{line}} = \mathcal{M}\kappa_e$, where $\mathcal{M}$ is force multiplier related to X-ray properties and κ_e is opacity due to electron scattering. The total radiation opacity therefore will be $(1+\mathcal{M})\kappa_e$, corresponding to a total radiation acceleration of $a_{\text{rad}} = (1+\mathcal{M})a_{\text{rad}}^{\text{es}}$.

From Stevens & Kallman (1990), The force multiplier can be parametrized as

$$\mathcal{M}\left(\tau_{\text{eff}}, \xi\right) = k\left(\xi\right)\tau_{\text{eff}}^{-0.6}\left[\frac{\left(1+\tau_{\text{eff}}\eta_{\max}(\xi)\right)^{0.4}-1}{\left(\tau_{\text{eff}}\eta_{\max}(\xi)\right)^{0.4}}\right] \approx k\left(\xi\right)\tau_{\text{eff}}^{-0.6} \tag{2.1}$$

where k and $\eta_{\max}$ are two fitting functions in Stevens & Kallman (1990), ξ is ionization parameter representing effect of X-rays and τ_{eff} is the effective optical depth parameter defined below. The dependences of $\mathcal{M}$, k and $\eta_{\max}$ on ξ are shown in Fig. 2.3. As can be seen, higher ξ will lead to lower k and $\eta_{\max}$ and therefore lower $\mathcal{M}$. This is happening when gas is too close to the centre. If ξ is not too large, one will see larger τ_{eff} lead to lower $\mathcal{M}$. With X-ray flux F_{X} and number density n of the gas, i.e. total number density, ξ is defined as

$$\xi = \frac{4\pi F_{\text{X}}}{n} \tag{2.2}$$

The X-ray flux is treated as coming from point source at centre of disk (representing corona). Therefore, at the position (R, z) in cylindrical polar coordinates, it is spherically symmetric and computed as

$$F_{\text{X}} = \frac{L_{\text{X}}\exp\left(-\tau_{\text{X}}\right)}{4\pi\left(R^2+z^2\right)} \tag{2.3}$$

where $L_{\text{X}} = f_{\text{X}}L_{\text{bol}}$ is the X-ray luminosity as a X-ray fraction f_{X} of bolometric

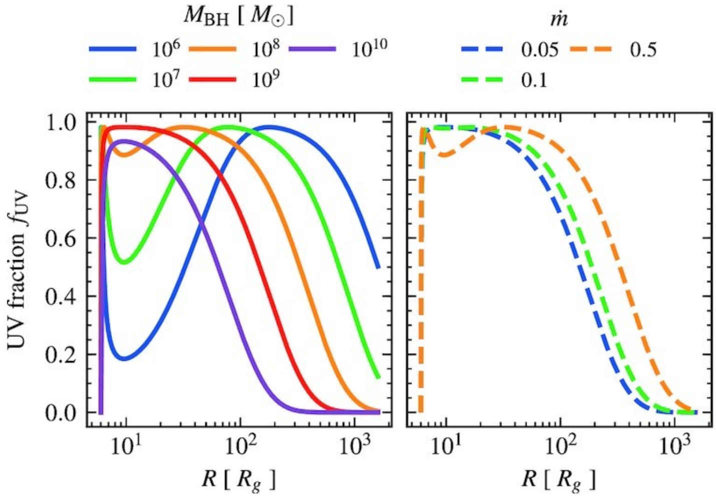

Figure 2.4: UV fraction as a function of disc radius with different black hole mass but fixed $\dot{m} = 0.5$ (left panel) or different Eddington ratio but fixed $M_{\mathrm{BH}} = 10^8 M_\odot$(right panel). Figure taken from Quera-Bofarull et al. (2023). **This figure shows UV fraction is higher at some radii, which related to M_{BH} and $\dot{m}$**

luminosity L_{bol} and τ_{X} is the X-ray optical depth.

The other variable in force multiplier, τ_{eff}, is defined as

$$\tau_{\mathrm{eff}} = \sigma_{\mathrm{T}} n v_{\mathrm{th}} |\frac{\mathrm{d}v}{\mathrm{d}l}|^{-1} \tag{2.4}$$

determined by thermal velocity $v_{\mathrm{th}} = \sqrt{k_{\mathrm{B}} T/(\mu m_{\mathrm{p}})}$ where mean molecular weight for fully ionized gas $\mu = 0.61$, k_{B} is the Boltzmann constant, and velocity gradient along the light ray $\mathrm{d}v/\mathrm{d}l$.

Next, I need to calculate $a_{\mathrm{rad}}^{\mathrm{es}}$, radiation acceleration due to electron scattering, to get total radiation force. Shakura & Sunyaev (1973) model is adopted for the emitted UV radiated power per unit area by a disc patch, which is

$$\mathcal{F}_{\mathrm{UV}} = \frac{3GM_{\mathrm{BH}}\dot{M}}{8\pi R_{\mathrm{d}}^3} f_{\mathrm{UV}}\left(R_{\mathrm{d}}\right) f_{\mathrm{NT}}\left(R_{\mathrm{d}}, R_{\mathrm{ISCO}}\right) \tag{2.5}$$

where R_{d} and R_{ISCO} is the radial position of the gas and the innermost stable radius of the black hole, respectively. f_{UV} is the UV fraction at this position and f_{NT} is the Novikov–Thorne relativistic factor (Novikov & Thorne, 1973). When considering non-rotating BHs, it can be expressed as

$$\begin{aligned} & f_{\mathrm{NT}}(a=0) \\ & = \frac{2r_{\mathrm{d}} - \sqrt{3r_{\mathrm{d}}}\left[2\sqrt{2} + \ln\left(3+2\sqrt{2}\right) + \ln\left(\sqrt{3r_{\mathrm{d}}}-3\right) - \ln\left(\sqrt{3r_{\mathrm{d}}}+3\right)\right]}{2\left(r_{\mathrm{d}}-3\right)} \end{aligned} \tag{2.6}$$

which increase from 0.11 to 0.88 when r_{d} increase from 10 to 1000. Here $r_{\mathrm{d}} = R_{\mathrm{d}}/R_{\mathrm{g}}$. With $\mathcal{F}_{\mathrm{UV}}$, the radiative acceleration due to electron scattering $a_{\mathrm{rad}}^{\mathrm{es}}$ can be calculated by

$$a_{\mathrm{rad}}^{\mathrm{es}}\left(R,z\right) = \mathcal{C}z \int\int \frac{f_{\mathrm{UV}} f_{\mathrm{NT}}}{R_{\mathrm{d}}^2 \Delta_{\mathrm{d}}^4} \exp -\tau_{\mathrm{UV}} \begin{pmatrix} R - R_{\mathrm{d}}\cos\phi_{\mathrm{d}} \\ -R_{\mathrm{d}}\sin\phi_{\mathrm{d}} \\ z \end{pmatrix} \mathrm{d}R_{\mathrm{d}}\mathrm{d}\phi_{\mathrm{d}} \tag{2.7}$$

where $\mathcal{C} = 3GM_{\mathrm{BH}}\dot{M}\kappa_e/(8\pi^2 c)$, $\Delta_{\mathrm{d}}^2 = R^2 + z^2 - 2RR_{\mathrm{d}}\cos\phi_{\mathrm{d}}$ and τ_{UV} is the UV electron scattering optical depth. The UV fraction f_{UV} is calculated by

$$f_{\mathrm{UV}}\left(R_{\mathrm{d}}\right) = \frac{\int_{E_1}^{E_2} \mathcal{B}\left(E, T(R_{\mathrm{d}})\right)\mathrm{d}E}{\int_0^{\infty} \mathcal{B}\left(E, T(R_{\mathrm{d}})\right)\mathrm{d}E} \tag{2.8}$$

where $\mathcal{B}(E,T)$ is the blackbody spectral radiance, $E_1 = 0.0038$keV and $E_2 = 0.06$keV, which are corresponding energy of the UV band (200-3200Å). The UV fraction as function of disc radius with different black hole mass or Eddington ratio is shown in Fig. 2.4. As one can see, all models have low f_{UV} when increasing radius since there are too low temperatures at large radii. Note that blackbody spectral radiance is a simplified approximation, which is not necessary true and realistic. Different SED models can be applied here to calculate more realistic UV fraction (Hagen & Done, 2023, Liang et al. in prep.).

Fig. 2.5 shows the radiation force due to electron scattering and force multiplier as function of radius. As one can see, the largest radiation force due to electron scattering and force multiplier occurs in the intermediate range, where winds are successfully launched. In contrast, for failed winds originating from the inner regions, the force multiplier is significantly weaker due to strong ionization. For failed winds from the outer regions, the radiation force from electron scattering is much weaker because of too few UV photons. In both cases, the total radiation force is insufficient to overcome the gravitational force. At this point, the radiation force can be determined to solve equations of motion for gas blobs and used to compute wind properties. Note that there are many details

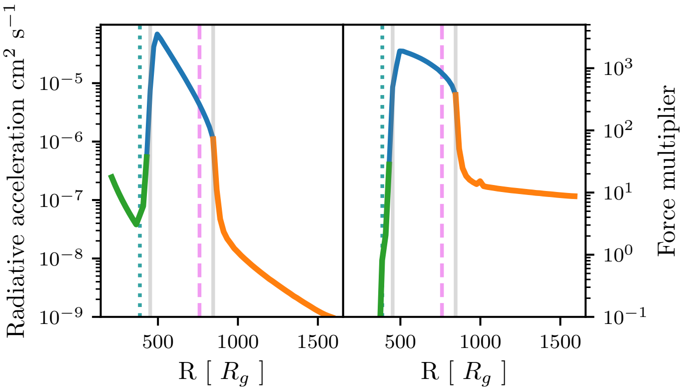

Figure 2.5: Maximum radiative force and force multiplier as a function of the initial radius of each streamline. Launched winds are within two vertical grey lines, require a balance between a sufficiently high-force multiplier (thus low ionization parameter) and a high radiative force. Gas trajectories originating at the green and orange radii will fall back to become failed winds. The radius at which the gas on the base of the wind becomes optically thick ($\tau = 1$) to X-rays and UV is denoted by the dotted blue and the dashed purple lines, respectively Figure taken from Quera-Bofarull et al. (2020). **This figure indicates at which radii the radiative acceleration is large enough to launch the wind succesfully and at which radii the wind failed due to small radiation force and small force multiplier.**

such as initial setup and parameters, gas launching, numerical method in calculating optical depth and solving equation of motions, as well as the construction of density interpolation grid, are omitted in this thesis since they are not directly related to the physical mechanism of line-driven wind.

2.2.2 Scaling relations

Using Qwind model, one can get several wind properties as output including mass outflow rate $\dot{M}_{\rm wind}$, kinetic luminosity $L_{\rm kin}$, momentum outflow rate $\dot{p}_{\rm wind}$, average outflow velocity $\langle v_r \rangle$, etc. $\dot{M}_{\rm wind}$ is calculated by summing outflow rate for all streamlines that escape to infinity, which can be integrated from $R_{\rm in}$ to $R_{\rm out}$ by

$$\dot{M}_{\rm wind} = 2 \int_{R_{\rm in}}^{R_{\rm out}} 2\pi R' \mu m_{\rm p} n \left(R'\right) v \left(R'\right) \mathrm{d}R' \tag{2.9}$$

where $n(R)$ and $v(R)$ are density and velocity when wind launched from sur-

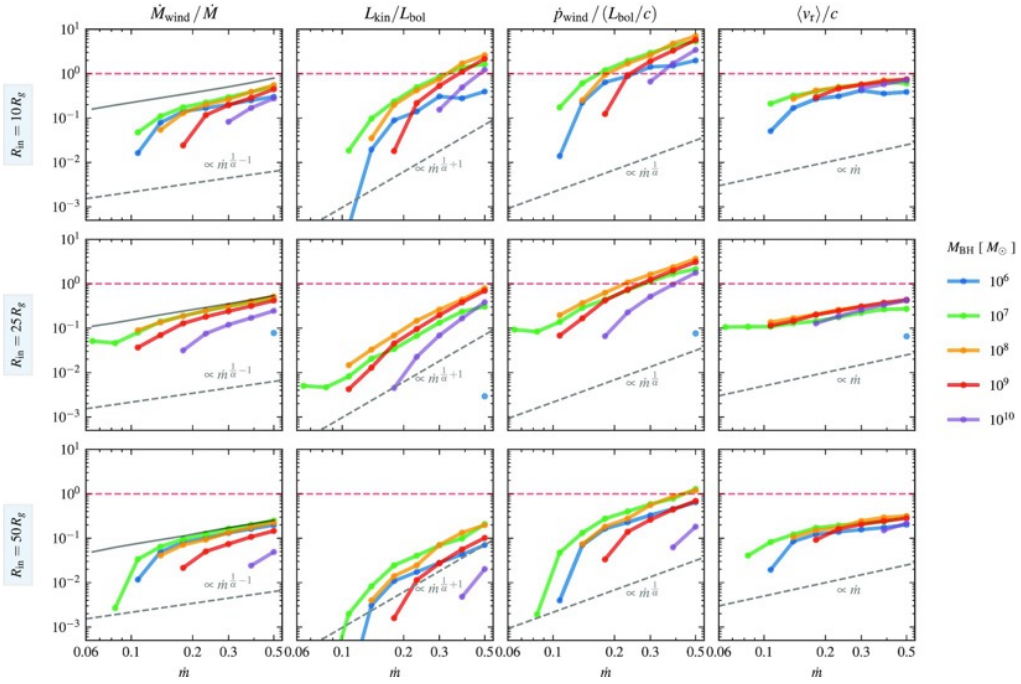

Figure 2.6: Wind mass-loss rate normalized by the mass accretion rate (first panel column), kinetic luminosity normalized by bolometric luminosity (second panel column), momentum loss rate normalized by $L_{\rm bol}/c$ (third panel column), and average velocity (fourth panel column) as functions of $\dot{m}$ for different $M_{\rm BH}$. The dashed grey lines show the scaling expected from the initial conditions and final velocity scalings. The solid grey lines in the first panel column delimit the maximum amount of mass that the wind can carry, given by the initial conditions. Figure taken from Quera-Bofarull et al. (2023). **This figure reveals that different BH properties are correlated to $\dot{m}$ by power laws.**

face of disk. The factor of 2 accounting for both sides of the accretion disc. With the outflow velocity of each streamline solved by equations of motion, one can get $L_{\rm kin}$ by summing $\dot{M}_{{\rm wind},i}v_{r,i}^2/2$ and $\dot{p}_{\rm wind}$ by summing $\dot{M}_{{\rm wind},i}v_{r,i}$ for all streamlines, where v_r is radial velocity at infinity. Then $\langle v_r\rangle$ can be obtained by $\sqrt{2L_{\rm kin}/\dot{M}_{\rm wind}}$. Normalized $\dot{M}_{\rm wind}$, $L_{\rm kin}$, $\dot{p}_{\rm wind}$, and $\langle v_r\rangle$ as functions of $\dot{m}$ with different $M_{\rm BH}$ and $R_{\rm in}$ are shown in Fig. 2.6. As one can see, normalized wind properties are in power-law correlation with $\dot{m}$ when $\dot{m} > 0.2$. They drop dramatically below this value because low initial density which correlated with $\dot{m}$ ($n_0 \propto \dot{m}^{1/\alpha}$ where $\alpha = 0.6$ is the slope, see Quera-Bofarull et al., 2023). As a consequence, the X-ray shielding would drop dramatically and strongly suppressing the wind. The dependence on $M_{\rm BH}$ is mainly from

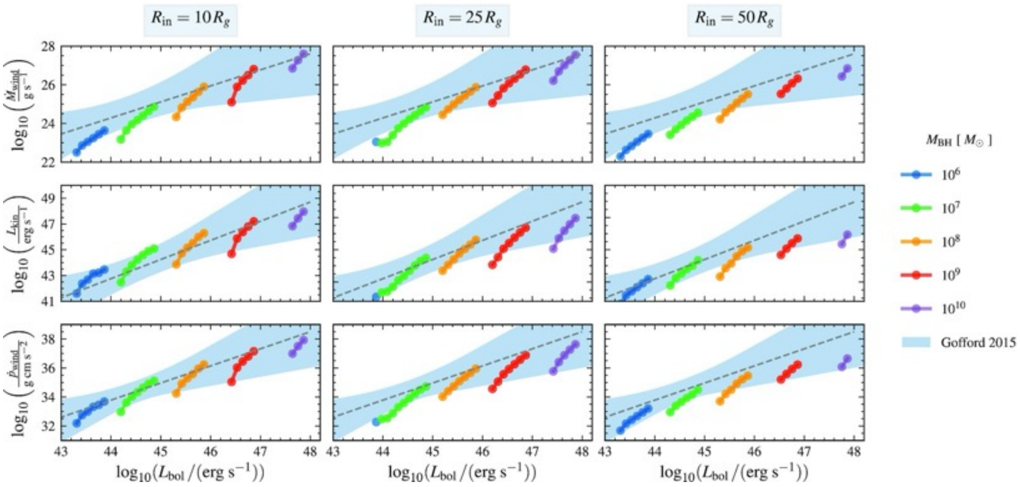

Figure 2.7: Comparison of Qwind results of mass-loss rate, kinetic luminosity, and momentum rate with the observations presented in Gofford et al. (2015) (dashed lines). The blue shadowed regions represent 90 per cent of the inferred posterior probability distribution parametrized following Nomura & Ohsuga (2017). Figure taken from Quera-Bofarull et al. (2023). **This figure shows that different properties predicted by Qwind lie in the range estimated from observations.**

UV fraction as shown in Fig. 2.4 and the reason why $\dot{M}_{\rm wind}/\dot{M}$ is in power-law correlation with $\dot{m}$ can be understood by using scaling relations of initial density and initial velocity. The initial density profile scales with $\dot{m}$ as $n_0 \propto \dot{m}^{1/\alpha}$ and the initial wind velocity scales with $\dot{m}$ as $v_0 \propto \dot{m}^{1/8}$. They imply that $\dot{M}_{\rm wind} \propto n_0 v_0 R^2 \propto \dot{m}^{1/8+1/\alpha} \approx \dot{m}^{1/\alpha}$, where I ignore 1/8 in the power since it is very small compared to $1/\alpha$. Then one can derive that $\dot{M}_{\rm wind}/\dot{M} \propto \dot{m}^{1/\alpha-1}$. With final velocity of the wind scales approximately $v_f \propto \dot{m}$, one can get scaling relations for $L_{\rm kin}/L_{\rm bol}$ and $\dot{p}_{\rm wind}/(L_{\rm bol}/c)$, although the detailed reason why I have such scaling relation for final velocity is still waiting to be found. The most significant scaling relation is that $L_{\rm kin}/L_{\rm bol} \propto \dot{m}^{2.6}$ since $L_{\rm kin}/L_{\rm bol}$ represents the coupling efficiency of AGN feedback. Currently, cosmological simulations such as EAGLE and IlustrisTNG calibrate coupling efficiency to try to reproduce observed stellar mass function of galaxies and assume a constant value of 0.15 (Schaye et al., 2015) or 0.1 (Weinberger et al., 2018) where the value of the constant is obtained by calibration. However, Qwind and other simulations (Nomura & Ohsuga, 2017) illustrates that this is not necessarily true. Although the slope and normalization of this scaling relation might depend on the details of the simulation and parameters, it is clear that $L_{\rm kin}/L_{\rm bol}$ as the coupling efficiency should be correlated with $\dot{m}$. This insight motivates the implementation a new AGN feedback model, where the coupling efficiency is no longer constant but instead varies with $\dot{m}$, following the form found in Qwind, though allowing different normalizations and slopes. Details of new implementation will be discussed in the next section.

Fig. 2.7 shows the comparisons of normalized $\dot{M}_{\rm wind}$, $L_{\rm kin}$, $\dot{p}_{\rm wind}$ as functions of $L_{\rm bol}$ with observational data (Gofford et al., 2015). As one can see that most of results are consistent with observation and RHD simulation, although they are slightly lower especially when $R_{\rm in} = 25R_{\rm g}$ or $R_{\rm in} = 50R_{\rm g}$. This is because higher $R_{\rm in}$ will decrease the amount of mass that can be potentially launched from disc due to smaller launching region and initial density. This parameter should be dependent on the structure of the accretion flow. The reason why it is treated as a free parameter is because Qwind lack such modeling, which can be implemented in the future. Note that this figure also suggest that normalized properties are dependent on $M_{\rm BH}$ and as a power law on $\dot{m}$, not just $L_{\rm bol}$.

2.2.3 Bug fixing and scaling relations revised

While Qwind successfully produces scaling relations which can be reasonable interpreteted and matched with observational data, I found several bugs. Although most of these issues involve missing or incorrectly added factors in the calculation of physical quantities, even minor errors can systematically shift the entire set of scaling relations. Therefore, the bug fixing is necessary in this work. Below, I present the identified bugs and the correction I made. Then I show the revised scaling relations compared with RHD simulation and observational data.

1. When defining Eddington luminosity Eq. (1.6), the code omit a factor of μ_e, where μ_e is set as 1.17 corresponding to a fully ionized gas with solar chemical abundance (Quera-Bofarull et al., 2023). Missing this factor would increase the value of the quantities that normalized by Eddington luminosity or Eddington accretion rate. The same issue arises when calculating the effective optical depth parameter.

2. When calculating wind properties, the both side of accretion disc should be accounted and multiply a factor of two wherever it needs. However, in Qwind, this factor is missed in some places such as such as mass loss

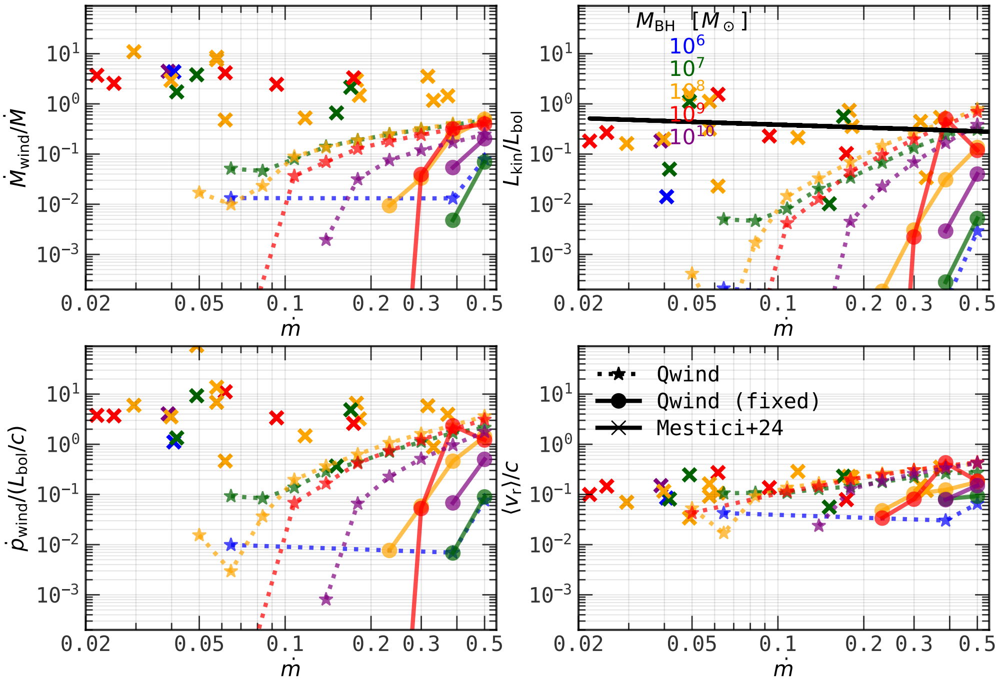

Figure 2.8: $\dot{M}_{\rm wind}$ normalized by the $\dot{M}$ (first panel), $L_{\rm kin}$ normalized by $L_{\rm bol}$ (second panel), $\dot{p}_{\rm wind}$ normalized by $L_{\rm bol}/c$ (third panel), and average velocity (fourth panel) as functions of $\dot{m}$ for different $M_{\rm BH}$. The dotted lines with stars represent the Qwind version from (Quera-Bofarull et al., 2023) while the solid lines with circles represent revised Qwind version using the same $R_{\rm in}$ (25 $R_{\rm g}$). Cross symbols stand for observational data from Mestici et al. (2024) and the black solid line is the best fit using all data. Colors mark different BH masses. **This figure indicates that the corrected version of Qwind show steeper relations and observations show flatter relations compared to the original version of Qwind.**

calculations Eq. (2.9) and when applying the mass loss kernel to compute line ranges. Correcting this ensures accurate estimates of wind properties.

3. When computing wind properties, there are inconsistencies in the coordinate system. For example, when calculate mass loss Eq. (2.9), the code should integrate the 2D projected radial position R instead of 3D radial position r. A similar error also exists when using mass conservation to calcualte number density in the streamlines. While the impact is minimal if the height above disc is negligible, I corrected this for accuracy.

4. In principle, the total number density should only be used when calculating

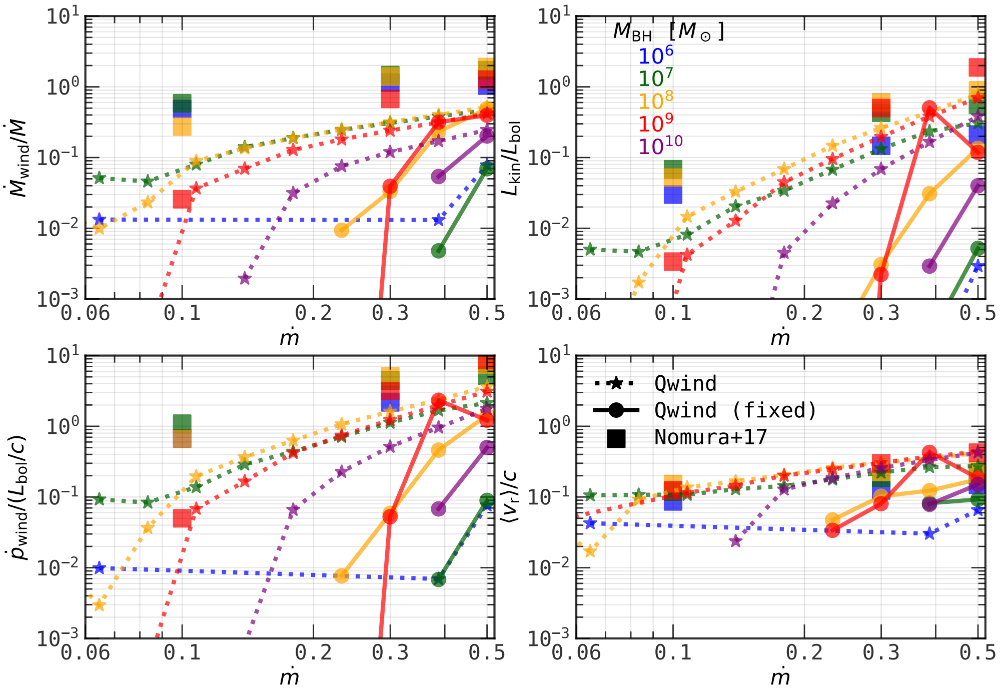

Figure 2.9: Similar to Fig. 2.8 but I compare Qwind result with the RHD simulation from Nomura & Ohsuga (2017) instead. **This figure shows that original Qwind results show similar slope in scaling relations as the RHD simulation while the corrected version of Qwind shows steeper slopes.**

ionization parameter while electron number density should only be used for other places. However, Qwind occasionally confused this with the electron number density, leading to errors in various calculations.

5. When computing ionisation parameter, a relativistic correction to the flux is missed. Although this correction is very small, it is better to keep it for physical completeness.

Using the corrected version of Qwind, I recalculated the wind properties and present the comparisons in Fig. 2.8, Fig. 2.9, and Fig. 2.10. As shown in Fig. 2.8 and Fig. 2.9, fixing the bugs significantly alters the scaling relations, leading scaling relations to be steeper and the normalization to be smaller. This means that the winds become weaker for the same black hole mass and the same Eddington ratio and more strongly correlated with $\dot{m}$. Furthermore, the minimum value of $\dot{m}$ required to launch winds become higher (~ 0.2) and there is no wind for black hole mass with $10^6 M_\odot$. Compared with RHD simulation in Fig. 2.9, it is

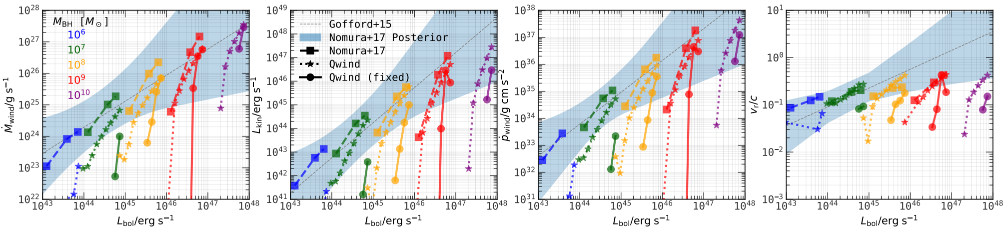

Figure 2.10: Comparison of scan results of mass-loss rate, kinetic luminosity, and momentum rate, velocity from different Qwind version with the observations presented in Gofford et al. (2015) and RHD simulation from Nomura & Ohsuga (2017). The dotted lines with stars represent the Qwind version from (Quera-Bofarull et al., 2023) while the solid lines with circles represent revised Qwind version. The blue shadowed regions represent the observational estimates from Gofford et al. (2015) which parametrized following Nomura & Ohsuga (2017) while the dash lines with squares represent their RHD simulation results. The grey dash lines represent the median relations from Gofford et al. (2015). **This figure indicates that when relating BH properties with L_{bol}, RHD simulation shows a good agreement with observation while original Qwind result within the range estimated from observations. As for fixed version, it show much lower values and steeper relations.**

surprisingly to see that revised version failed to match them well especially for normalized $\dot{M}_{\mathrm{wind}}$, L_{kin}, $\dot{p}_{\mathrm{wind}}$, but the original version can. As seen in Fig. 2.10, the original Qwind results and RHD simulation data fall within the distribution of observational data, while the revised version of Qwind can only predict smaller value for all quantities. In addition, they also show steeper relations with L_{bol}. These findings suggest that while the bug fixes improve internal consistency, the Qwind model still lacks crucial physical ingredients. If no more bugs exist in Qwind, these discrepancies highlight the need to incorporate additional physical processes to produce more realistic predictions, which shall be the future work. Compared with observation data in Fig. 2.8, one can see that while the Qwind results can match $\langle v_{\mathrm{r}} \rangle / c$, the observation actually is showing negative slope in other relations especially for $L_{\mathrm{kin}}/L_{\mathrm{bol}} - \dot{m}$ relation.

2.2.4 Future work

Although revised Qwind results show the qualitatively similar trends with the original Qwind results, the RHD simulation (Nomura & Ohsuga, 2017) and observational data (Gofford et al., 2015), revised Qwind results do not reproduce them well. Therefore, it is worth noting that there are some simplified assumption which could possibly influence the results. Firstly, Qwind assume constant f_{X}. However, observation show that this could be coupled with Eddington ratio by $f_{\mathrm{X}} = 0.02/\dot{m}$ (Kubota & Done, 2018). The implementation of this can lead higher f_{X} at low $\dot{m}$ regime and lower f_{X} at high $\dot{m}$ regime, which will make scaling relations steeper. Secondly, black body spectral radiance is too simple for accretion disc. The implementation of more sophisticated SED model will make the code more physical. Thirdly, the code assume the spin of BH is zero and the influence of non-zero spin can also be studied. The spin mainly influence the radiative efficiency and f_{NT}, potentially will lead to different scaling relations. Finally, from Fig. 2.6 Fig. 2.7 the normalization and slope is not the same for different M_{BH} and $\dot{m}$ and maybe f_{X}, a, if I consider different values of them. In principle, one can get other scaling relations with varying normalization and slopes by exploring parameter space. These improvements will be done in my future work

Chapter 3

Idealized simulations of disc galaxies

In this chapter, I will briefly introduce the simulation code and the subgrid physics used to run the idealized simulations. I will then explain how the new AGN model is implemented, motivated by the previous chapter. Finally, I will describe the initial setup for the idealized runs.

3.1 `SWIFT`-COLIBRE code

The idealized simulations in this thesis use the open source simulation code `SWIFT`[1] (Schaller et al., 2024). `SWIFT` is a fully public code that integrates cosmology, gravity, hydrodynamics, and galaxy subgrid model such as radiative cooling, star formation, chemistry, and feedback from stars and black holes, using task-based parallelism. The equations of hydrodynamics are solved using the smoothed particle hydrodynamics (SPH) method (Monaghan, 1992) and the default hydrodynamical scheme is `SPHENIX` (Borrow et al., 2022). The gravitational force is computed by using fast multipole method (FMM Greengard & Rokhlin, 1987) coupled with a particle-mesh method solved in Fourier space.

The updated subgrid models from the COLIBRE project (Schaye et al., in prep.) are implemented in `SWIFT` and will be used in this thesis. Below, I will provide some details of its BH model and briefly introduce subgrid models for other compoenents.

The radiative cooling and heating rate are taken from tabulated tables

---

[1] www.swiftsim.com

(Ploeckinger & Schaye, 2020), using radiative transfer code `CLOUDY` (Ferland et al., 2017), combing with with non-equilibrium chemical network (CHIMES, Richings et al., 2014a,b, 2022), covering wide range of density, temperature, chemical composition and redshift of gas. The star formation model in COLIBRE combines a Schmidt law with a gravitational instability criterion (Nobels et al., 2024) rather than relying on traditional density and temperature thresholds. The core-collapse supernova (CCSN) feedback model in COLIBRE (Chaikin et al., 2023) builds upon stochastic kinetic and thermal models used in `OWLS` (Schaye et al., 2010) and `EAGLE` (Schaye et al., 2015) simulation, respectively. The energy release from Type-Ia supernova (SNIa) feedback is following the same algorithm as the CCSN feedback but operates only through thermal channel. The implementation of early stellar feedback will be detailed in Ploeckinger et al (in preparation) accounting for processes including H_{II} regions, stellar winds, and radiation pressure using the Binary Population and Spectral Synthesis (`BPASS`) tables (Eldridge et al., 2017; Stanway & Eldridge, 2018). The stellar evolution and chemical enrichment models for CCSN, SNIa, stellar-winds and asymptotic giant branch stars are based on Wiersma et al. (2009) as well as neutron star mergers, common envelope jets supernovae and collapsars channels are considered in COLIBRE to track the evolution of 12 elements: H, He, C, N, O, Ne, Mg, Si, Fe, Sr, Ba, Eu.

3.1.1 Black holes and AGN feedback

The model of supermassive black hole (SMBH) growth and AGN feedback in COLIBRE is based on Booth & Schaye (2009) with several developments including BH repositioning, nibbling (Bahé et al., 2022), variable heating temperatures. It also includes spin-driven jet feedback (Huško & Lacey, 2023a,b; Huško et al., 2024) as an optional choice, although not used in this work.

In COLIBRE, as in most of other simulations, a SMBH with mass m_{seed} is seeded by converting the densest gas particle when the host halo reaches a total mass exceeding a threshold M_{FOF}. The choice of m_{seed} and M_{FOF} depend on resolution and have a large effect in low-mass galaxies, which need to be calibrated. Note that in our idealized simulations, black hole seeding is not used since I only need to place a SMBH with inputed mass.

After initialising a BH, it grows continuously by accreting gas from their surroundings. In COLIBRE, Bondi-Hoyle-Lyttleton model (Hoyle & Lyttleton, 1939; Bondi & Hoyle, 1944) limited by Eddington rate is adopted

$$\dot{M} = \min\left[\alpha_{\rm BH}\frac{4\pi G^2 M_{\rm BH}^2\rho_{\rm gas}}{\left(c_{\rm s}^2 + v_{\rm gas}^2\right)^{3/2}}, \dot{M}_{\rm Edd}\right] \tag{3.1}$$

where $c_{\rm s}$ is the sound speed of the ambient gas and $v_{\rm gas}$ is the bulk velocity of the gas relative to the SMBH. The boost factor $\alpha_{\rm BH}$ is dependent on the gas density by

$$\alpha_{\rm BH} = \max\left[\alpha(n_{\rm H}/n_{\rm H}^{\star})^{\beta}, \alpha\right] \tag{3.2}$$

where $n_{\rm H}^{\star}$, α and β are free parameters. Note that in our idealized simulations, I set $n_{\rm H}^{\star} = 10^{10}$ cm^{-3}, $\beta = 1$ and $\alpha = 0.2$ to force $\alpha_{\rm BH} = 0.2$. This accretion model lead to a growth of SMBH with a minimum e-folding time (for BH accreting at Eddington limit) of 45Myr. A fraction $\epsilon_{\rm r} = 0.1$ of total accreted mass over timestep Δt is converted to energy and the left will be added to SMBH mass by nibbling algorithm (Bahé et al., 2022).

COLIBRE models AGN feedback by an isotropic thermal mode and a jet kinetic mode. The jet mode is not included here because I only want to study winds behaviours. Therefore, I simply introduce thermal mode here, which is intended to represent effect of small-scale, fast winds from AGN since the kinetic energy released by winds can eventually present as thermal energy by thermalizing and interacting with gas through shocks and turbulence. In thermal mode, the SMBH inject energy with a rate $\dot{E} = \epsilon_r \eta \dot{M} c^2$ into the surrounding gas with coupling efficiency $\eta = 0.1$ (for the standard COLIBRE model). AGN heat gas particles by a temperature increment $\Delta T_{\rm AGN}$ corresponding to a energy

$$\Delta E_{\rm heat,AGN} = \frac{k_{\rm B}\Delta T_{\rm AGN}}{\gamma - 1}\frac{\langle m_{\rm ngb}\rangle}{\mu m_{\rm p}} \tag{3.3}$$

where $\langle m_{\rm ngb}\rangle$ is the mean mass of gas particles within the BH kernal. Typically $\int_t^{t+\Delta t}\dot{E}{\rm d}t \ll \Delta E_{\rm heat,AGN}$, the model store $\int_t^{t+\Delta t}\dot{E}{\rm d}t$ in energy reservoir $E_{\rm BH}$ until $E_{\rm BH} \geq N_{\rm heat}\Delta E_{\rm heat,AGN}$ where Δt is a single BH timestep, $N_{\rm heat}$ is the minimum number of heating event in a AGN feedback event as a free parameter and large value lead to more explosive and bursty feedback. If this is satisfied, SMBH will heat up surrounding particles by $\Delta T_{\rm AGN}$.

There are some parts of the COLIBRE BH evolution model that are not used in this work. First, in addition to gas accretion, the other way to allow SMBH to grow in cosmological simulation is merger. When two SMBHs approach each other, they lose orbital energy through dynamical friction or three-body encounters. Since there is only one BH in idealized simulation, the BH cannot grow by this way. Another update to SMBH model is repositioning (Bahé et al., 2022). This model select surrounding gas calculate the lowest gravitational potential in that region and move SMBH to that position if its current potential larger than the value. Note that repositioning is not used in our idealized simulations. Instead, I force the black hole to stay in the box centre.

3.2 Implementation of new AGN model

Motivated by Qwind model and observation that discussed in Chapter 2, I implement a new model for coupling efficiency in COLIBRE. Instead of directly adopting the normalization N_η and slope α_η from Qwind, I keep these two as free parameters. This is due to the potential dependence of these parameters on the specifics of the line-driven wind model, which would benefit from calibration. The variable coupling efficiency therefore takes form of

$$\eta = \min\{N_\eta \dot{m}^{\alpha_\eta}, 1\} \tag{3.4}$$

which can be re-written as

$$\log \frac{\eta}{0.1} = \min\{\log \frac{N_\eta}{39.81} + \frac{\alpha_\eta}{2.6} \log \left(\frac{\dot{m}}{0.1}\right)^{2.6} + (2.6 - \alpha)\, , 1\} \tag{3.5}$$

This expression highlights that when the parameters $N_\eta = 39.81$ and $\alpha_\eta = 2.6$ (the slope revealed in Quera-Bofarull et al. (2023)) I will have $\eta = 0.1$ when $\dot{m} = 0.1$. This parameter option is motivated by observational data (Mestici et al., 2024) as one can see in Fig. 2.8. Based on this option, I have two varying methods. The first one is varying one parameter while the other one fixed. The other choice is requiring $\eta = 0.1$ when $\dot{m} = 0.1$, which will yield $N_\eta = 39.81 \times 10^{\alpha_\eta - 2.6}$. It is worth noting that a shorter timestep is necessary when calculating BH quantities to use this variable coupling efficiency model. Otherwise, there will be two possible issues arised: (1) the AGN energy input saved in the output files might be inconsistent with the energy calculate from a time integral over the accretion rate ($\int \eta \epsilon_{\rm r} \dot{M} c^2 {\rm d}t$) due to the accretion history is not properly resolved; and (2) a gas particle might be overheated ($\sim 10^{12}$K) due to the energy input being overestimated. In COLIBRE, the timestep for BH is calculated by $\Delta t = \Delta E_{\rm heat,AGN}/\dot{E}_{\rm heat,AGN}$, where $\dot{E}_{\rm heat,AGN} = \epsilon_{\rm r}\eta\dot{M}c^2$ is the instantaneous AGN energy injection rate. Therefore, to address these issues, I modify this by setting a high heating rate with $\dot{E}_{\rm heat,AGN} = \epsilon_{\rm r}\dot{M}_{\rm Edd}c^2$, only when calculate the BH timestep. In the next chapter, convergence tests will demonstrate the effectiveness of this solution.

3.3 Simulation setup

I simulate idealized disky galaxy consisting of an exponential disc of stars and cold gas (with no stellar spheroid) embedded in a hot CGM under a static DM halo potential. The disky galaxy is also MW-like since it has similar components with similar masses. I also set similar temperatures and metallicity for the gas. The initialization of discs and DM follows Nobels et al. (2024), which based on `MAKENEWDISK` code from Springel et al. (2005) while the distribution of the hot CGM is modeled by similar ways as Nobels et al. (2022). Specifically, I allow an initial dynamical relaxation phase for the CGM in the non-spherical potential due to the disk (see below), which the latter is new for `SWIFT`. All parameters are summarized in Table 3.1.

3.3.1 Dark matter halo

In `MAKENEWDISK`, the static dark matter halo follows a Hernquist profile (Hernquist, 1990) profile which takes form of

$$\rho_{\rm DM}\,(r) = \frac{M_{\rm DM}}{2\pi}\frac{r_{\rm s}}{r(r+r_{\rm s})^3} \tag{3.6}$$

where $M_{\rm DM}$ is the total mass of DM obtained by integrating $\rho_{\rm DM}$ to infinity and $r_{\rm s}$ is scale radius where the logarithmic density slope equal to -2, i.e. $\mathrm{d}\log\rho_{\rm DM}/\mathrm{d}\log r = -2$. To set the halo mass in more usual way, I use virial mass M_{200} to define density profile, where M_{200} is the mass within virial radius R_{200}, the radius within which the average density of the halo is 200 times the critical density of the universe, i.e. $M_{\rm vir} = 4\pi\Delta_c\rho_c R_{\rm vir}^3/3$, where $\Delta_c = 200$ is the overdensity factor and ρ_c is the critical density. Then, using $M_{200} = \int_0^{R_{200}} \rho_{\rm DM} 4\pi r^2 \mathrm{d}r$,

Component	Parameters					
DM halo	Profile	$M_{200}/M_\odot$	R_{200}/kpc	r_s/kpc	c	λ
	Hernquist	1.37×10^{12}	228	25.3	9	0.033
Cold gas disc	Profile	$M_\mathrm{d,gas}/M_\odot$	$R_\mathrm{0,gas}$/kpc	$z_\mathrm{0,gas}$/kpc	$Z/Z_\odot$	$T_\mathrm{0,gas}$/K
	Exponential	5.48×10^{9}	4.3	0.43	1	10^4
Stellar disc	Profile	$M_{\mathrm{d},*}/M_\odot$	$R_{0,*}$/kpc	$z_{0,*}$/kpc		
	Exponential	4.932×10^{10}	4.3	Hydro Equilibrium		
Hot CGM	Profile	$M_\mathrm{CGM}/M_\odot$	r_0/kpc	T_0/K	$Z/Z_\odot$	λ'
	Numerical	9.3×10^{10}	3.5	10^6	0.3	0.05
SMBH	$M_\mathrm{BH}/M_\odot$	η	N_η	α_η	Comments	
	$10^6, 4 \times 10^6, 10^7, 10^8, 10^9$	$\eta = N_\eta \dot{m}^{\alpha_\eta}$	39.81	2.6	Fiducial	
	$10^6, 4 \times 10^6, 10^7, 10^8, 10^9$	$\eta = 0.1$	NA	NA	Default constant	
	$10^6, 10^7, 10^8$	$\eta = N_\eta \dot{m}^{\alpha_\eta}$	39.81	0.5,1.5,2,3	Variation for variable η	
	$10^6, 10^7, 10^8$	$\eta = N_\eta \dot{m}^{\alpha_\eta}$	10,100,300,3000	2.6	Variation for variable η	
	$10^6, 10^7, 10^8$	$\eta = N_\eta \dot{m}^{\alpha_\eta}$	$N_\eta = 39.81 \times 10^{\alpha_\eta - 2.6}$	0.5,1.5,2,3	Variation for variable η	
	$10^6, 10^7, 10^8$	$\eta = 0.01, 1$	NA	NA	Variation for constant η	

Table 3.1: Parameters for initializations of DM halo, cold gas disc, stellar disc, hot CGM and SMBH used in this thesis. The parameters for all components except SMBH are the same for all runs. For SMBH, I show different variations for N_η, α, corresponding η, and the BH mass that applied.

one can rewrite Hernquist profile as

$$\rho_{\mathrm{DM}}(r) = \frac{M_{200}(R_{200}+r_{\mathrm{s}})^2}{2\pi R_{200}^2} \frac{r_{\mathrm{s}}}{r(r+r_{\mathrm{s}})^3} \tag{3.7}$$

Based on cosmological N-body simulations of the DM evolution, the DM density profile is better reproduced by Navarro, Frenk & White profiles (Navarro et al., 1997, hereafter NFW), which is

$$\rho_{\mathrm{NFW}}(r) = \frac{M_{200}}{4\pi R_{200}^3} \frac{1}{f(c)\, x\, (c^{-1}+x)^2} \tag{3.8}$$

where $f(c) = \ln(1+c) - \frac{c}{1+c}$, $x = r/R_{200}$ and $c = R_{200}/r_{\mathrm{s}}$ is the NFW concentration. Therefore, to better match NFW profile with Hernquist profile, I constrain the central part of DM density profile by

$$\rho_{\mathrm{DM}}(r) = \rho_{\mathrm{NFW}}(r) \tag{3.9}$$

With the assumption that $r_{\mathrm{s}}/R_{200} \ll 1$, this implies

$$r_{\mathrm{s}} = \frac{b+\sqrt{b}}{1-b} R_{200} \tag{3.10}$$

where $b = 2f(c)/c^2$. Since R_{200} can be determined by M_{200} (given $H_0 = 70.4$ km/s/Mpc), one only needs to set NFW concentration to define a DM profile. In all runs, I choose a halo virial mass $M_{200} = 1.37 \times 10^{12} M_{\odot}$ and a NFW concentration $c = 9$, which are typical values for MW-like galaxies. The angular momentum of DM halo is initialized by dimensionless spin parameter $\lambda \equiv J|E|^{1/2}/GM_{200}^{5/2}$ where J is the magnitude of DM angular momentum and E is the total energy of DM measured with R_{200}. In all runs, the spin parameter is set to $\lambda = 0.033$.

3.3.2 Stellar disc and cold gas disc

The profiles of stellar disc and cold gas disc are represented by

$$\rho_{\mathrm{d}}(R,z) = \frac{M_{\mathrm{d}}}{4\pi z_0 R_0^2} \mathrm{sech}^2\left(\frac{z}{2z_0}\right) \exp\left(-\frac{R}{R_0}\right) \tag{3.11}$$

where the disc mass is set to 4 percent of the virial mass, $M_{\mathrm{d}} = 5.48 \times 10^{10} M_{\odot}$. The cold gas disc mass takes up 10 percent of total disc, $M_{\mathrm{d,gas}} = 5.48 \times 10^{9} M_{\odot}$

while the remainder is stellar disc, corresponding to $M_{\mathrm{d},*} = 4.932 \times 10^{10} M_{\odot}$. R_0 and z_0 is scale radius and scale height for the disc, respectively. I follow the scenario in Mo et al. (1998), which yields a disc scale radius $R_0 = 4.3$kpc.

Specifically, Mo et al. (1998) calculates the angular momentum of the halo by

$$J = \lambda G^{1/2} M_{200}^{3/2} R_{200}^{1/2} \left(\frac{2}{g_c} \right)^{1/2} \tag{3.12}$$

where g_c is a function related to concentration c by

$$g_c = \frac{c \left[1 - 1/(1+c)^2 - 2\ln(1+c)/(1+c) \right]}{2 \left[\ln(1+c) - c/(1+c) \right]^2} \tag{3.13}$$

Then the angular momentum of the disc can be calculated by

$$J_{\mathrm{d}} = M_{\mathrm{d}} \int_0^{\infty} V_{\mathrm{c,d}}(R) \left(\frac{R}{R_0} \right)^2 \exp\left(-\frac{R}{R_0} \right) \mathrm{d}R \tag{3.14}$$

where $V_{\mathrm{c,d}}$ is the circular velocity of the disc given by

$$V_{\mathrm{c,d}}^2(R) = \frac{G M_{\mathrm{DM}}(< R)}{R} + \frac{2 G M_{\mathrm{d}}}{R_0} y^2 \left[I_0(y) K_0(y) - I_1(y) K_1(y) \right] \tag{3.15}$$

Here $y = R/(2R_0)$ and the I_n and K_n are Bessel functions. With the assumption that J_d is proportional to J, one can relate R_0 to λ and solve R_0 numerically given other quantities, i.e. $M_{200}, R_{200}, c, M_{\mathrm{d}}$, are determined.

Although both discs have the same scale radius set above, their scale heights are different. The stellar scale height is fixed as 10 percent of scale radius, $z_0 = 0.43$kpc, while the scale height of gas is determined by hydrostatic equilibrium. I assume solar metallicity for initial cold gas disc and its initial temperature is 10^4K. The stellar velocity distribution at each position can in principle be determined by solving collisionless Boltzmann equation based on density profile. In practice, I approximate this by imposing a 3D Gaussian velocity distribution for the stars at each location, with 2nd moments calculated using the following procedure, based on the equations of stellar hydrodynamics, which are moments of the Boltzmann equation. In `MAKENEWDISK`, mixed second-order moments of velocity distribution are set to 0. Non-vanishing dispersions in radial direction and vertical direction are set as follows:

$$\langle v_z^2 \rangle = \frac{1}{\rho_\mathrm{d}} \int_z^\infty \rho_\mathrm{d} \left(z', R\right) \frac{\partial \Phi}{\partial z'} \mathrm{d}z' \tag{3.16}$$

Φ is the potential from total mass components. There is good observational evidence that $\langle v_R^2 \rangle$ is proportional to $\langle v_z^2 \rangle$ for stellar disc. The initial condition therefore assume that $\sigma_R^2 = \langle v_R^2 \rangle = f_R \langle v_z^2 \rangle$ where $f_R = 1$. Note that our initial condition for discs are adopted from Nobels et al. (2022) and add a CGM manually later. Therefore, the total potential used to set up the initial conditions is only consisted of DM, stellar disc and cold gas disc. The corresponding parts in azimuthal direction are set by

$$\langle v_\phi^2 \rangle = \langle v_R^2 \rangle + \frac{R}{\rho} \frac{\partial \left(\rho \langle v_R^2 \rangle\right)}{\partial R} + v_c^2 \tag{3.17}$$

where $v_c^2 = R \partial \Phi / \partial R$ is the circular velocity. In `MAKENEWDISK`, it is assumed that the first moments in radial and vertical direction vanished, i.e. $\langle v_R \rangle = \langle v_z \rangle = 0$. Then, one can get dispersions in radial and vertical direction by $\sigma_{R,z}^2 = \langle v_{R,z}^2 \rangle$.

For stellar disc, the code employs the epicycle approximation for dispersion in azimuthal direction expressed as

$$\sigma_\phi^2 = \frac{\sigma_R^2}{\kappa^2} \tag{3.18}$$

where

$$\kappa^2 = \frac{4}{R} \frac{\partial \Phi}{\partial R} \left(\frac{3}{R} \frac{\partial \Phi}{\partial R} + \frac{\partial^2 \Phi}{\partial R^2} \right) \tag{3.19}$$

Using σ_ϕ^2 in Eq. (3.18), one can get mean azimuthal velocity

$$\langle v_\phi \rangle = \left(\langle v_\phi^2 \rangle - \frac{\sigma_R^2}{\kappa^2} \right)^{1/2} \tag{3.20}$$

With given $\sigma_R, \sigma_\phi, \sigma_z, \langle v_R \rangle, \langle v_\phi \rangle, \langle v_z \rangle$, the velocity distribution of stellar disc for all direction can be determined.

For cold gas disc, Eq. (3.17) cannot be used. Instead, azimuthal velocity of cold gas disc should be replaced by the radial balance between gravity and,

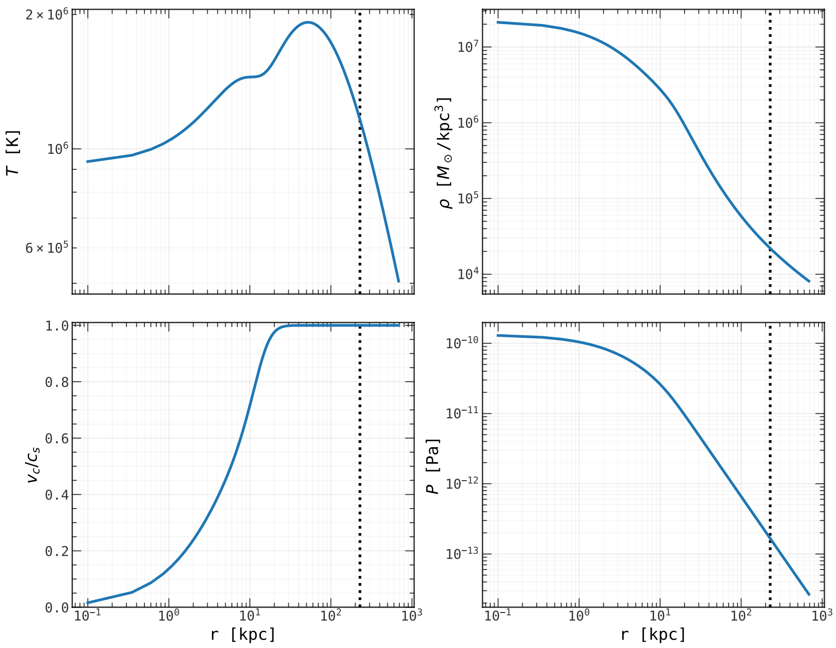

Figure 3.1: The initial temperature, density, velocity, pressure profile of CGM in this thesis using the initialization method from Nobels et al. (2022). For all panels, I adapt $T_0 = 10^6$ K, r_0=3.5 kpc. The black dotted lines represent R_{200}. **This figure shows the results from initialization method.**

centrifugal and pressure support, which takes form of

$$v^2_{\phi,\mathrm{gas}} = R\left(\frac{\partial\Phi}{\partial R} + \frac{1}{\rho_{\mathrm{d,gas}}}\frac{\partial P}{\partial R}\right) \tag{3.21}$$

3.3.3 Circumgalactic medium

From observations, there are clear evidences that our MW and other similar galaxies are surrounding by hot CGM. Therefore, it is necessary and realistic to construct CGM after initializing DM, stellar disc and cold gas disc. However, it is not easy to achieve equilibrium for all components at the beginning, due to discs are not spherical symmetric. To solve this issue, I adapt formalism in Nobels et al. (2022), where they construct a system with a spherical CGM in dynamical equilibrium in the gravitational potential generated by a static DM, stellar components following spherical distribution, to create CGM particles and then add them into the initial condition. Note that, our stellar distribution is exponential disc but I neglect the difference for simplicity, which means that I treat mass distribution of disc as spherical only for calculating its gravitational potential when setting up initial spherical CGM distribution, not afterwards. The initial temperature, density, velocity and pressure profile can be seen in Fig. 3.1. I derive the initialization for these profiles below.

The CGM is assumed initially to be in hydrostatic equilibrium and in a spherical potential,

$$\frac{\mathrm{d}P}{\mathrm{d}r} = -\frac{GM_{\mathrm{en}}\left(r\right)\rho\left(r\right)}{r^2} \tag{3.22}$$

where M_{en} is enclosed mass from DM and stellar disc, ignoring CGM itself. Since the density of CGM should be quite low compared to DM, its contribution to enclosed mass is neglected. The equation above can be rewritten as

$$\frac{\mathrm{d}\ln P}{\mathrm{d}\ln r} = -\gamma\frac{v_c^2}{c_s^2} \tag{3.23}$$

where $c_s = \sqrt{\gamma P/\rho}$ is local sound speed and $\gamma = 5/3$ is the adiabatic index of the gas. Under the assumption of $c_s = v_c$, this corresponds to

$$P = P_0\left(\frac{r}{r_0}\right)^{-\gamma} \tag{3.24}$$

where P_0 is normalization. One can get temperature profile given gravitational bound solutions that $c_s = v_c = k_{\mathrm{B}}\gamma T/\mu m_p$

$$T_{\mathrm{circ}} = \frac{\mu m_{\mathrm{p}}}{k_{\mathrm{B}}\gamma}\frac{GM_{\mathrm{en}}\left(r\right)}{r} \tag{3.25}$$

where $\mu = 0.6$ is the mean particle mass for fully ionized gas, k_{B} is the Boltzmann constant and m_{p} is the proton mass. All derivation are based on $v_c = c_s$. However, this assumption breaks in the galaxy centre where $v_c = 0$ lead to $T = 0$, which is unrealistic. Therefore, one needs to modify temperature profile by imposing a temperature floor

$$T_{\mathrm{tot}} = T_{\mathrm{circ}} + \frac{T_0}{1+\exp\left(\frac{r-2r_0}{r_0}\right)} \tag{3.26}$$

with central temperature T_0 and scale radius r_0, as two free parameter. With this temperature profile, one can inversely solve eq. (3.23) instead of using eq. (3.24), although numerically. Then one can get corresponding density profile by $\log n(r) = \log P(r) - \log k_{\mathrm{B}}T(r)$ and sample CGM particles where the unit of

n, P, k_B, T are cm^{-3}, 0.1 Pa, erg/K, and K, respectively. In this model, T_0, r_0 and total mass within R_{200} are free parameters. In all runs, T_0 is set to 10^6 K while r_0 is set to 3.5kpc. The total mass within R_{200} is $M_\mathrm{CGM} = 9.3 \times 10^{10} M_\odot$, which is 6.8 percent of M_{200}. The initial metallicity of CGM is one third of solar metallicity.

The initial velocity structure of CGM is assumed to follow rotation-only scheme, although CGM rotational velocity is ignored when setting up initial CGM density profile, which is spherical. The magnitude of rotation velocity v_rot is based on CGM specific angular momentum distribution (j_CGM) and spherical radial dependence ($v_\mathrm{rot} = j_\mathrm{CGM}/r$) within R_{200} but with a slightly different spin parameter of the gas ($\lambda' = 0.05$). The j_CGM is obtained by using the fitting functions from Bullock et al. (2001) which expressed as

$$j_\mathrm{CGM} = j_0 \frac{M_\mathrm{en}(r)}{M_{200}} \frac{1}{\mu'_\lambda - M_\mathrm{en}(r)/M_{200}} \tag{3.27}$$

where the first parameter μ'_λ is set as 1.25 and the second parameter j_0 is calculated by

$$j_0 = \frac{\sqrt{2} V_{200} R_{200} \lambda'}{-\mu_{\lambda'} \ln(1 - \mu_{\lambda'}^{-1}) - 1} \tag{3.28}$$

where $V_{200} = \sqrt{G M_{200}/R_{200}}$ is the virial velocity. Note that different from Bullock et al. (2001), the enclosed mass here is for stars and DM instead of DM-only. The scheme to setting the rotational velocity of the CGM is identical to that in Nobels et al. (2022), except that the stellar density profile is for a disk instead of a spheroid. To sample CGM particles and achieve dynamical equilibrium with other components, based on the model above from Nobels et al. (2022) and Nobels et al. (2024), I first initialize a stellar disc and a CGM distribution with a static DM halo, characterized by its mass, concentration, and spin. I then simulate the system with hydrodynamics and gravity for 3 Gyr, turning off stellar feedback, AGN feedback, gas cooling, star formation and other subgrid physics model. From the last snapshots, I extract the CGM distribution, add a black hole of varying mass, replace the time-evolved stellar disc with the initial one, i.e. before running for 3 Gyr, and introduce a cold gas disc to construct the ICs for our idealized simulations.

These steps ensure the system (including CGM) reaches a good approximation to dynamical equilibrium before turning on all of the subgrid gas physics for

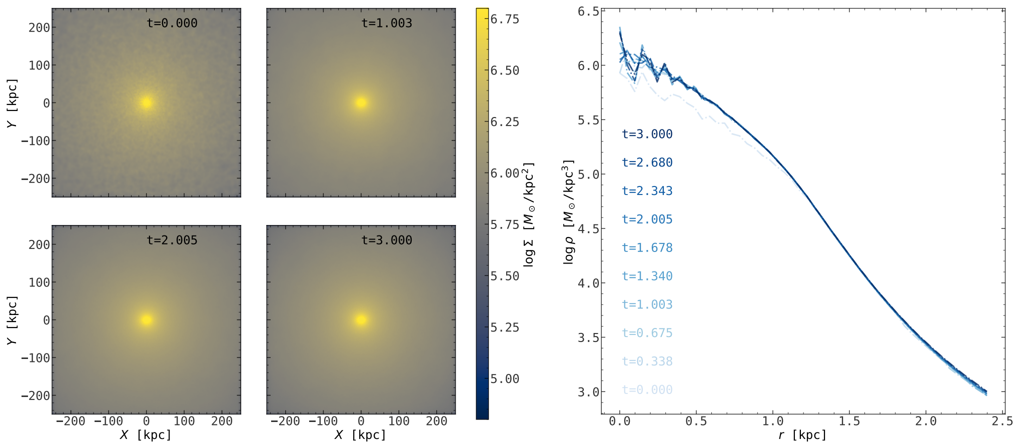

Figure 3.2: The density maps as well as density profiles of CGM in our gravity and hydrodynamics only simulation at different cosmic time. Face-on maps are represented in the left small panels while the density profiles are represented right big panel. The time interval in maps is ∼1 Gyr while the time interval in profile panel is ∼0.3 Gyr. Edge-on maps are similar with the face-on panels. **This figure indicates that the density profile of CGM reach equilibrium after running gravity and hydro only simulation for quite a lot less than 3 Gyr (~ 0.3 Gyr).**

cooling, star formation, feedback, etc. If the CGM were added directly, the system would not be fully in dynamical equilibrium. Running the simulation with only gravity and hydrodynamics helps achieve a stable dynamical equilibrium state. I initially exclude the cold gas disc to prevent energy exchange between it and the hot CGM, which would otherwise heat the gas disc and prevent it from remaining cold in the ICs. Additionally, the stellar disc dominates the disc potential, meaning the absence of the cold gas disc during gravity and hydrodynamics only simulation has a minimal effect on achieving system's dynamical equilibrium and CGM's distribution.

The surface density maps and temperature maps as well as their radial profile are shown in Fig. 3.2 and Fig. 3.3. As one can see that the density and temperature of CGM reach equilibrium very soon (∼0.3 Gyr for density while ∼2 Gyr for temperature) then stay stable.

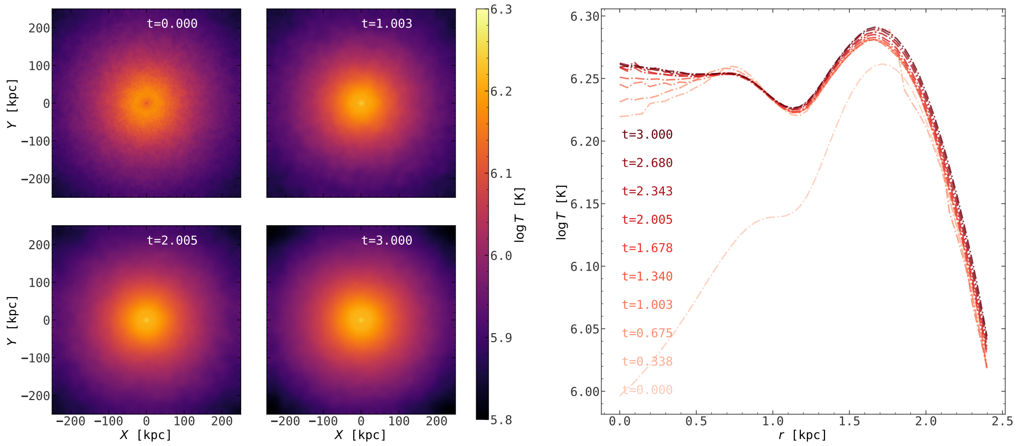

Figure 3.3: Similar to Fig. 3.2 but for temperature maps and profiles. **This figure indicates that the temperature profile of CGM reach equilibrium after running gravity and hydro only simulation for 3 Gyrs.**

3.3.4 Supermassive black hole

For all simulations, the setup for components described above (DM halo, stellar disc, cold gas disc and hot CGM) remains consistent. For BH, I pin them in the box centre and vary their masses across different values: $M_{\rm BH} = (10^6, 4\times 10^6, 10^7, 10^8, 10^9)M_\odot$. The choice of $4\times10^6 M_\odot$ is specially to match the observed MW BH mass (Event Horizon Telescope Collaboration et al., 2022) while the other BH masses cover the range of observed BH masses for Milky Way mass disky galaxies ($1.14\times10^6 M_\odot$ - $8.97\times10^8 M_\odot$, Table 3 in Kormendy & Ho, 2013). Two options for $\Delta T_{\rm AGN}$ can be used: one is with fixed temperature increment, $\Delta T_{\rm AGN} = 10^9$K while the other one is followed by floor-limited power law depending on, $\Delta T_{\rm AGN} = \min[10^{6.5}{\rm K}, 10^{10}{\rm K}(M_{\rm BH}/10^9 M_\odot)^{2/3}]$. While both options are calibrated to reproduce observation relations in COLIBRE cosmological simulations, the second option is especially motivated a few points below:

1. It allows sampling well AGN feedback in low-mass galaxies
2. It makes feedback more gentle in low-mass galaxies and galaxies at early times, which means that the model needs to use higher seed masses. At high resolution cosmological runs, with constant $\Delta T_{\rm AGN}$, the seed mass was very low (of order 100 $M_\odot$), with essentially no growth in low-mass galaxies ($M_* < 10^{10} M_\odot$), resulting in no BH of appreciable mass in such galaxies.

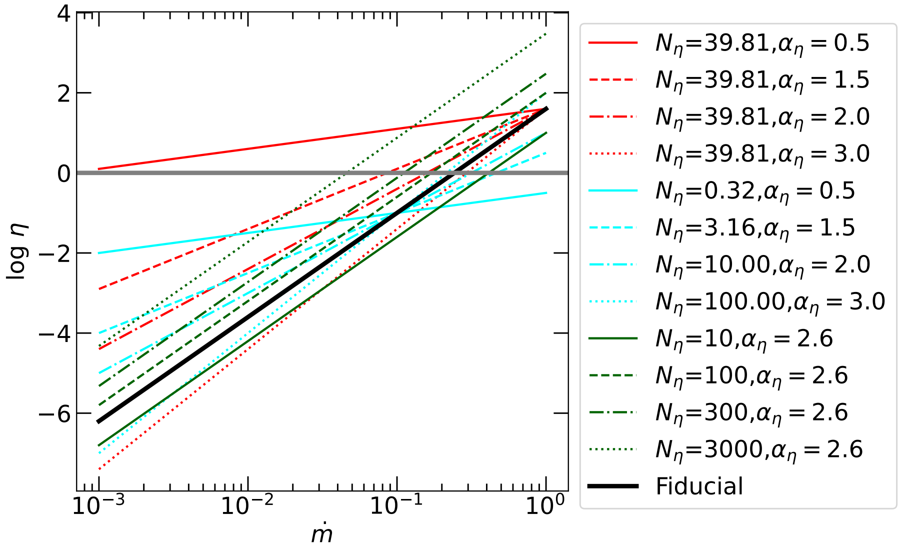

Figure 3.4: The coupling efficiency η as function of the Eddington ratio $\dot{m}$, using our variable coupling efficiency model with different parameters as different linestyles and colors show. The fiducial parameters are $N_\eta = 39.81$ and $\alpha_\eta = 2.6$. The horizontal gray line represent the ceiling. All η above this line will be set as unity. **This figure shows how η is changed with different N_η and α_η**

Once galaxies reached a mass around $10^{10} M_\odot$, their BHs experienced very bursty growth and settled onto the established (and observed) $M_{\rm BH}$ - M_* relation. However, with variable $\Delta T_{\rm AGN}$, the entire $M_{\rm BH}$ - M_* relation is more smooth, with the seed mass of order $3 \times 10^4 M_\odot$ or more at all resolutions.

3. It allows higher heating temperatures in galaxy clusters, which may help with stopping cooling flows and quenching brightest cluster galaxies

Note that larger values will make individual feedback events more energetic and more intermittent. In this thesis, for each BH mass, constant $\Delta T = 10^9$ K is chosen as fiducial setting since I only want to study the influence from coupling efficiency on galaxy and feedback properties. Regarding the coupling efficiency η, two approaches are tested: one is constant efficiency, $\eta = 0.1$ and the other one is variable coupling efficiency depending on $\dot{m}$ as mentioned before. For the fiducial setup, I use the parameters $N_\eta = 39.81$ and $\alpha_\eta = 2.6$, which yield $\eta = 0.1$ when $\dot{m} = 0.1$. Additionally, I also run some simulations with two parameter variation methods. The first one is varying $N_\eta = 10, 100, 300, 3000$

while keeping $\alpha_\eta = 2.6$, as well as with varying $\alpha_\eta = 0.5, 1.5, 2, 3$ while fixing $N_\eta = 39.81$. The other one is fix $\eta = 0.1$ for $\dot{m} = 0.1$ as varying α_η These settings are for $M_{\rm BH} = 10^6, 10^7, 10^8 M_\odot$ cases. In Fig. 3.4, I show how η change as N_η and α_η varying. For fixing $N_\eta = 39.81$ but α_η varying cases, all model lead to $\eta = 39.81$ when $\dot{m} = 1$. For cases using dependent N_η and α_η, all lines reach (0.1,0.1) in $\dot{m} - \eta$ plane. One thing worths to be noted is when α_η becomes very small (0.5) but N_η is not set to be small accordingly, the corresponding η will be larger than 1 for $\dot{m} > 10^{-3}$. Similar thing can be seen when N_η becomes very large (3000) but α_η is not set to be large accordingly, the corresponding η will be larger than 1 for $\dot{m} \gtrsim 10^{-1}$. These provide some constrains for N_η and α_η since too large η for relatively small $\dot{m}$ is not physical.

Chapter 4

Results

In this chapter, I show the results in terms of feedback properties, and galaxy properties with different simulations. In feedback properties, I will use cumulative AGN energy input E_{AGN}, AGN energy injection rate $\dot{E}_{\mathrm{AGN}}$, Eddington ratio $\dot{m}$, coupling efficiency η, BH mass scaled by initial BH mass $M_{\mathrm{BH}}/M_{\mathrm{BH,0}}$ to demonstrate model differences. In galaxy properties, I will show their performances in star formation rate (SFR), cold gass mass M_{cold}, mass outflow rate $\dot{M}_{\mathrm{out}}$, energy outflow rate $\dot{E}_{\mathrm{out}}$, net mass outflow rate $\dot{M}_{\mathrm{net}}$, net energy outflow rate $\dot{E}_{\mathrm{net}}$.

In Fig. 4.1, the temperature maps show that the fiducial variable coupling efficiency model yield weaker feedback strength compared to default constant coupling efficiency model since default model can heat up surrounding gas to higher temperatures, especially for high mass black hole mass where AGN feedback are playing an important role. I will further investigate this in the following sections.

4.1 Feedback properties

In Fig. 4.2, I compare the feedback properties between fiducial variable coupling efficiency model, i.e. $\alpha_\eta = 2.6$ and $N_\eta = 39.81$ in eq. (3.4), and default constant coupling efficiency with $\eta = 0.1$. In the top left panel, where I compare E_{AGN}, one can see that low mass BHs will lead to weak but frequent AGN feedback event while high mass BH tend to strongly blow a large amount of gas at the beginning. This can also be seen in the top right panel where I show that low mass BHs fluctuate more for AGN energy injection rate. Also, from these two panels, I see that higher BH masses lead to higher energy values across all models. This

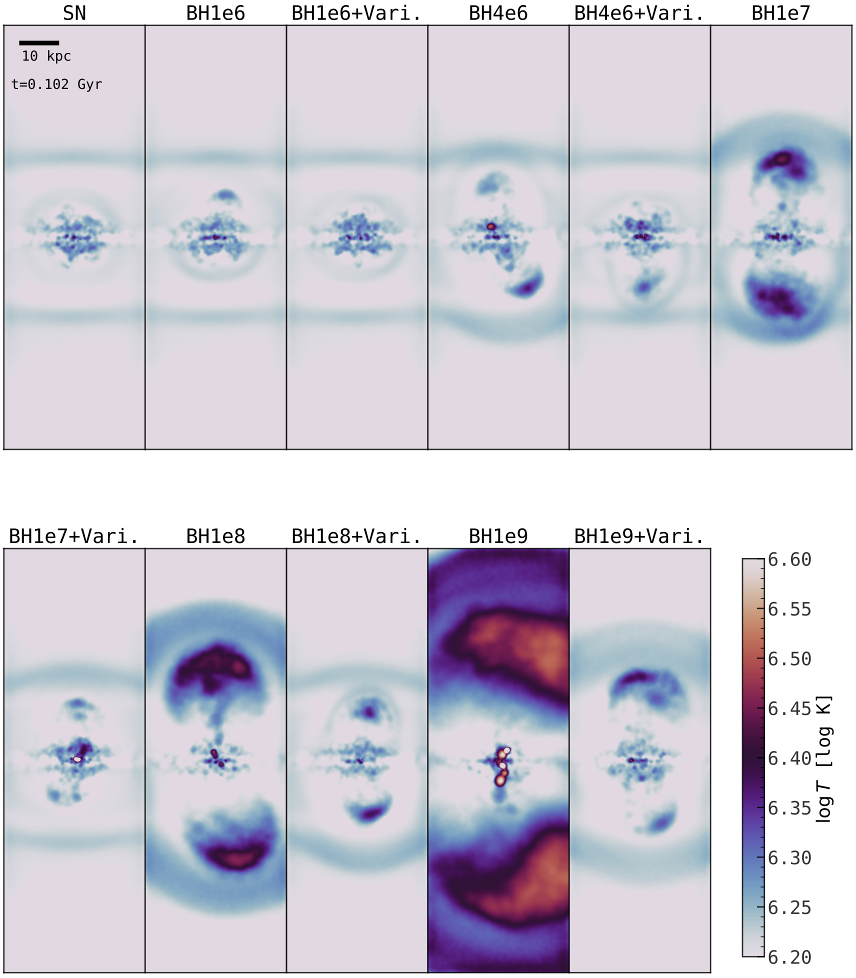

Figure 4.1: Edge-on projected temperature maps at $t \sim 0.1$Gyr for no AGN run, constant coupling efficiency runs and fiducial variable coupling efficiency runs as the title of each panel shows. The darker, the higher temperature, as the color bar marks. **This figure shows that higher BH masses lead to more explosive AGN feedback while fiducial variable coupling efficiency model lead to weaker AGN feedback.**

correlation is expected since higher BH masses lead to higher accretion rates (see eqs. (3.1)), and the corresponding AGN energy will be higher ($E_{\rm AGN} = \int \epsilon_r \eta \dot{M} c^2 {\rm d}t$), provided constant or similar η. Consequently, more gas is accreted onto the BH, and more energy accumulates in the energy reservoir for the next or future feedback events. However, fiducial varying efficiency models show that the difference in energy and energy rate diminishes with increasing mass. For

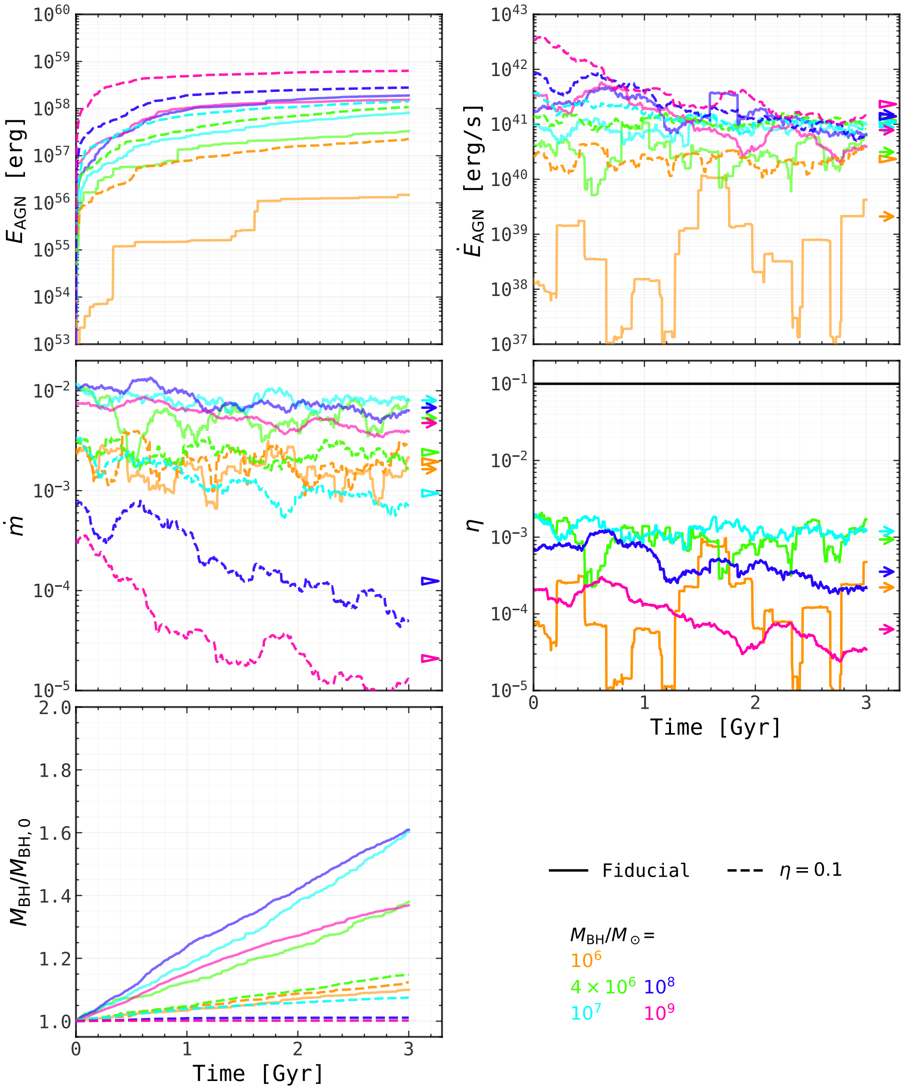

Figure 4.2: Feedback property comparisons between fiducial variable coupling efficiency model and constant coupling efficiency model $\eta = 0.1$. Each panel shows a comparison in different feedback properties including $E_{\rm AGN}$, $\dot{E}_{\rm AGN}$, $\dot{m}$, η, $M_{\rm BH}/M_{\rm BH,0}$. The black hole masses vary across different values and represented by different colors: 10^6 (orange), 4×10^6 (green), 10^7 (cyan), 10^8 (blue), 10^9 (magenta). The fiducial models are shown by solid lines while the dash lines represent constant coupling efficiency model. The horizontal black line in middle right panel represent default constant value for coupling efficiency, i.e. $\eta = 0.1$. The arrows (fiducial) or wedges ($\eta = 0.1$) in the right of the panel stand for the median values averaged by the last 2 Gyr. **This figure indicates that fiducial variable coupling efficiency lead to less explosive AGN feedback, lower η, higher accretion rate and faster BH growth. Additionally, this model enhances self-regulation.**

$M_{\rm BH} = 10^8 M_\odot$ and $M_{\rm BH} = 10^9 M_\odot$ cases, the difference become negligible small while the default constant coupling efficiency models maintain a factor of two difference between these mass scales. This might indicate the BH self-regulations which means that feedback power remains similar across different black hole masses, likely because higher accretion rates and corresponding AGN energy rate affect surrounding gas properties (e.g., reducing gas density). Eventually, these factors ultimately compensate and lead to similar feedback power. This is especially clear in high BH mass cases since their AGN feedback are playing more important roles.

In the second row, I compare $\dot{m}$ and η, where η is dependent on $\dot{m}$ for our variable coupling efficiency models. The $\dot{m}$ trends differ markedly between variable and constant efficiency models. For variable coupling efficiency models, I see that higher BH masses generally lead to higher $\dot{m}$, with $M_{\rm BH} = 10^9 M_\odot$ case showing a slight small value. Conversely, the default constant coupling efficiency models exhibit an inverse relationship, where higher BH masses yield smaller $\dot{m}$. This can be understood by the scaling relations among $\dot{m}$, $M_{\rm BH}$ and $\rho_{\rm gas}$. From eqs. (3.1), one can obtain $\dot{m} \propto M_{\rm BH}\rho_{\rm gas}/(c_{\rm s}^2 + v_{\rm gas}^2)^{3/2}$. After a strong feedback event, particularly in high mass BH cases, the gas is expelled, leading to higher velocity and smaller density, which will suppress accretion in the subsequent timestep. If the feedback power remain in a comparatively strong level, i.e. $\eta = 0.1$ cases, the accretion rate will be smaller in the future due to persistently lower gas density with fewer gas falling back. In that case, $\rho_{\rm gas}$ is dominant since it potentially drop more than an order of magnitude. Nevertheless, in our variable η cases, η and the feedback power connected to η in the next timestep is dependent on the current $\dot{m}$. If the accretion rate is lower due to smaller gas density after a feedback, the η will be smaller as well. Since the values of η are much smaller compared to $\eta = 0.1$, as I see in the middle right panel, more gas will eventually fall back and fuel the BH, leading to higher accretion rates. In that case, $M_{\rm BH}$ is dominant in $\dot{m}$ instead. As a consequence, the variable coupling efficiency models will lead to faster BH growth due to this higher accretion rate as one can see in the last panel.

Next, based on the fiducial models, I explore variations in the normalization N_η and slope α_η, comparing their results with the same quantities. In addition, for a given BH mass, I compare these variations with fiducial model and constant coupling efficiency model with higher value ($\eta = 1$) or lower value ($\eta = 0.1$). I

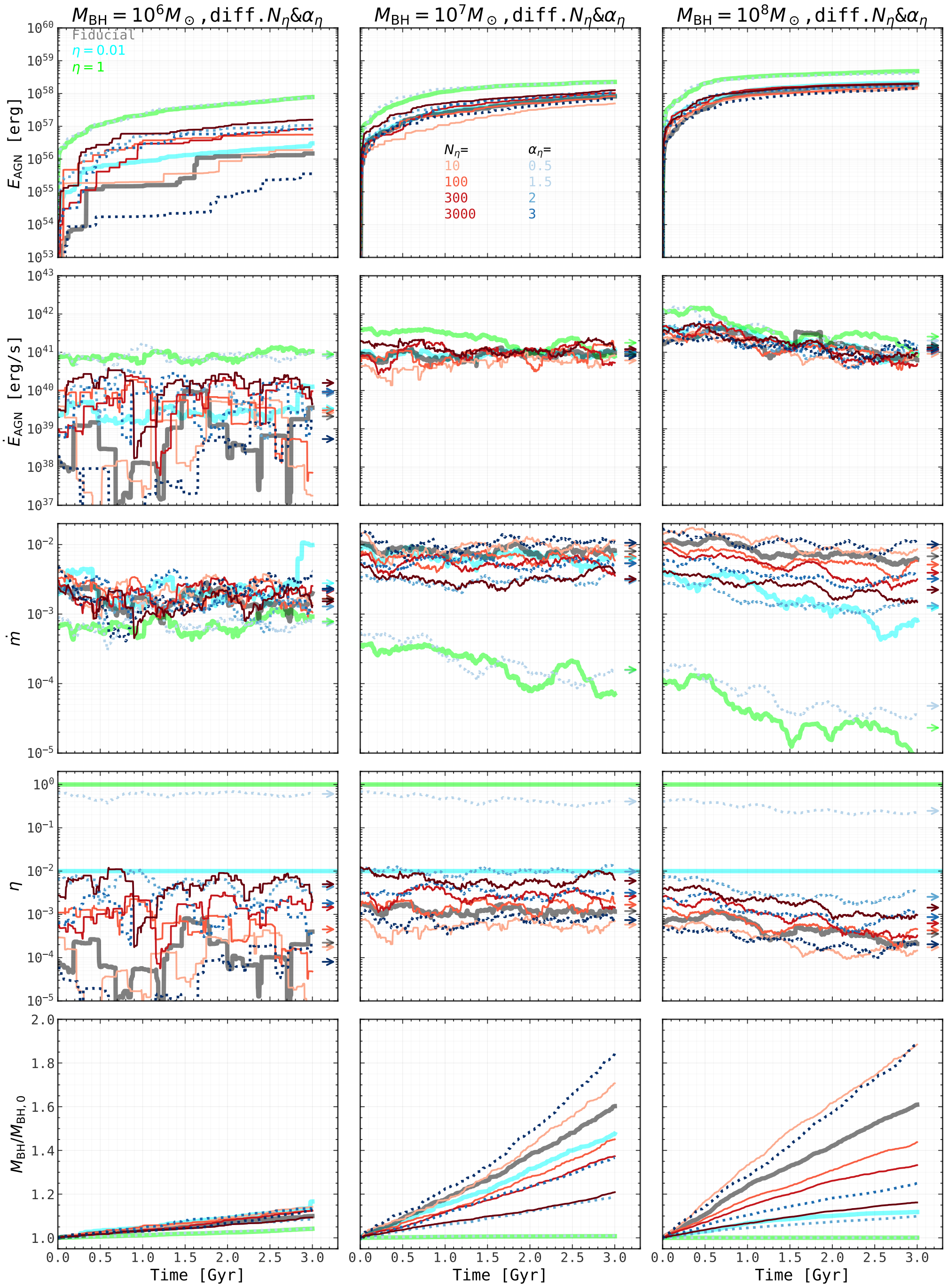

Figure 4.3: Feedback property comparisons for variable coupling efficiency models varying N_η or α_η while fixing the other. Each row shows a comparison in different feedback properties including E_{AGN}, $\dot{E}_{\text{AGN}}$, $\dot{m}$, η, $M_{\text{BH}}/M_{\text{BH},0}$. Each column stand for a black hole mass. The red solid lines represent models varying N_η ($N_\eta = 10, 100, 300, 3000$) while fixing α_η. The blue dotted lines represent models varying α_η ($\alpha_\eta = 0.5, 1.5, 2, 3$) while fixing N_η. The darker, the higher values for N_η or α_η as the top middle panel shows. The arrow with the same color scheme in the right represent the median values averaged by the last 2 Gyr. In all panels, I show three references models with the same BH masses: fiducial model (gray), low constant coupling efficiency model ($\eta = 0.01$, cyan), high constant coupling efficiency model ($\eta = 1$, green). **This figure indicates that higher η (lower α_η or higher N_η) lead to stronger AGN feedback, higher accretion rate and faster BH growth accordingly.**

first vary either the N_η or the α_η while keeping the other fixed, with the results presented in Fig. 4.3. In $E_{\rm AGN}$ and $\dot{E}_{\rm AGN}$ shown in the first and second rows, lower α_η or higher N_η, with the other fixed, lead to higher $E_{\rm AGN}$ or $\dot{E}_{\rm AGN}$. although it is a minor change for $M_{\rm BH} = 10^7 M_\odot$ and $M_{\rm BH} = 10^8 M_\odot$ cases, it is significant for $M_{\rm BH} = 10^6 M_\odot$ cases, where variations in N_η and α_η lead to differences of several orders of magnitude. This behavior is explained in the third and fourth panels, which display the trend of $\dot{m}$ and η. As one can see in these two rows, lower α_η or higher N_η lead to lower $\dot{m}$ and higher η at the same BH mass. For $M_{\rm BH} = 10^6 M_\odot$, while the differences in $\dot{m}$ are small, there are a few orders of magnitude differences when varying N_η and α_η. The result for $\alpha_\eta = 0.5$ is even 10^2 to 10^4 larger than other results varying α_η. As a consequence, higher η will lead to higher $E_{\rm AGN}$ and $\dot{E}_{\rm AGN}$ ($E_{\rm AGN} = \int \epsilon_r \eta \dot{M} c^2 {\rm d}t$). The reason why the results with $M_{\rm BH} = 10^7 M_\odot$ and $M_{\rm BH} = 10^8 M_\odot$ are very close is because the difference in $\dot{m}$ and η tend to compensate, resulting in similar values of $E_{\rm AGN}$ and $\dot{E}_{\rm AGN}$. This compensation highlights self-regulation at high BH masses. The trend in the last row, where I show BH mass increase, follow the same trend in accretion rate. Comparisons with three reference models: fiducial model, constant coupling efficiency model with higher value ($\eta = 1$) or lower value ($\eta = 0.01$), show that their behaviors are also dominated by η. Note that the fiducial model is lies between other variable models with variations and high value constant efficiency model is very close to variable coupling efficiency model with $\alpha_\eta = 0.5$ in all panels due to close η value.

The other variation method sets $\eta = 0.1$ when $\dot{m} = 0.1$, yielding $N_\eta = 39.81 \times 10^{\alpha_\eta - 2.6}$ (see Section 3.2). I keep the same range of α_η values as in Fig. 4.3 and determine the corresponding N_η values. I show and compare the results with this variation in Fig. 4.4. Compared to Fig. 4.3, the differences between models in $E_{\rm AGN}$ and $\dot{E}_{\rm AGN}$ are smaller, as seen in the first and the second row. And higher BH mass tend to show smaller differences. This again, because η and $\dot{m}$ are better compensated or BH self-regulation is happening, leading to similar energy. The systematics here is lower α_η will lead to higher η, smaller $\dot{m}$ and higher AGN energy, although it is not clear due to compensation.

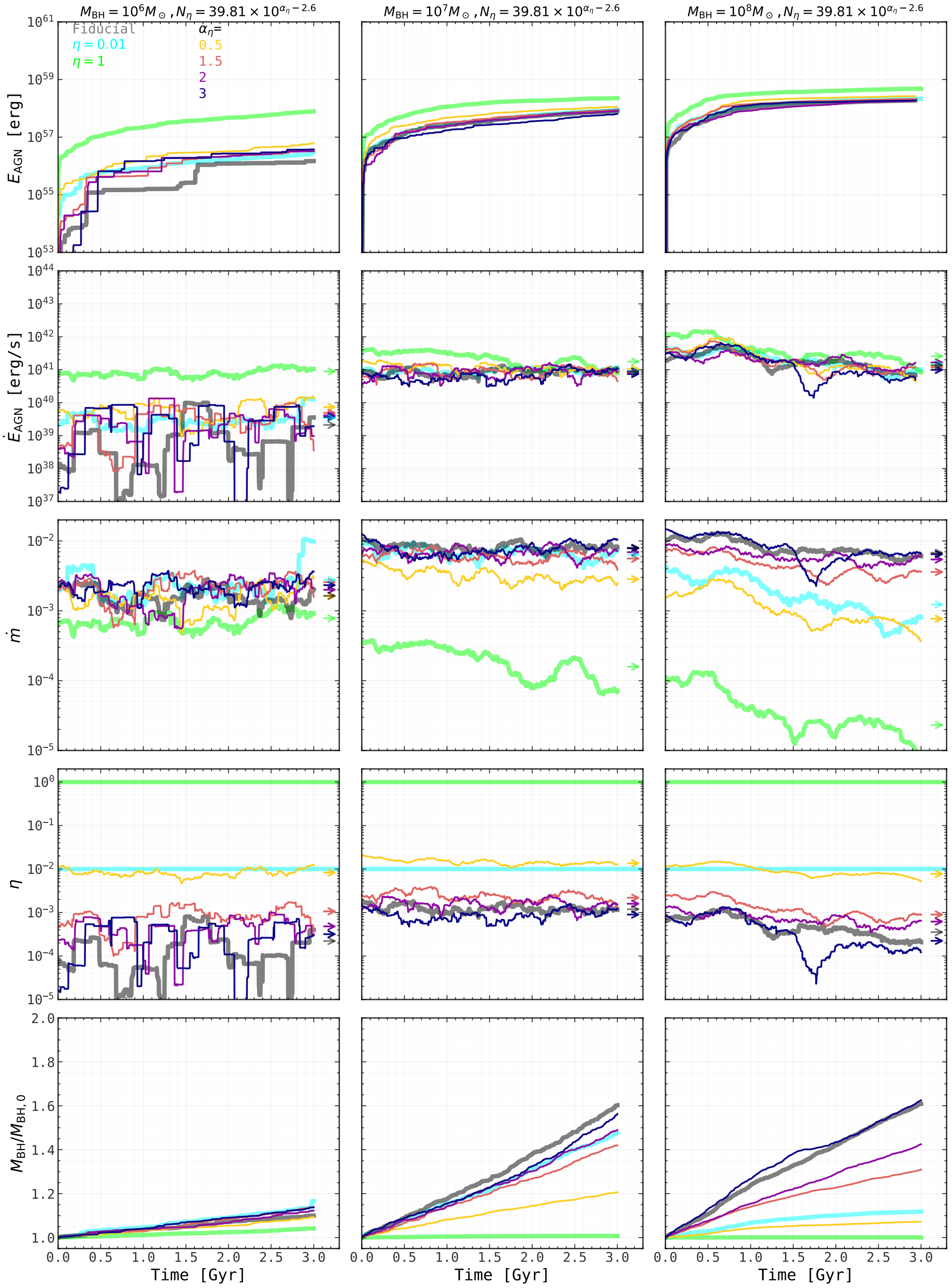

Figure 4.4: Similar to Fig. 4.3 but I show the comparison between variable coupling efficiency models varying normalization and slope following $N_\eta = 39.81 \times 10^{\alpha_\eta - 2.6}$. Each color represent a α_η as the top left panel shows, while N_η are therefore determined. **This figure indicates that for dependent N_η and α_η, lower α_η lead to higher η, which result in higher AGN energy and energy rate but smaller accretion rate and slower BH growth.**

4.2 Galaxy properties

Now I move on to compare galaxy properties. Starting with the SFR, as it provides the most direct evidence of how AGN feedback influences galaxy growth. As one can see from Fig. 4.5, both the constant coupling efficiency model and the fiducial variable coupling efficiency model produce results with low mass BHs ($M_{\rm BH} = 10^6, 4\times10^6 M_\odot$) similar to SN only run, which means that AGN feedback plays a negligible role in such systems. In contrast, for intermediate to high mass BHs ($M_{\rm BH} \geq 10^7 M_\odot$) cases, SFR is suppressed due to more powerful and efficient AGN feedback. Comparing both models, the SFR of the fiducial variable coupling efficiency model tends to be slightly higher, implying that its role in surpressing galaxy growth is less pronounced. This difference can be understood by AGN energy released as shown in Fig. 4.2 where the fiducial variable coupling efficiency models tend to release fewer energy. However, despite this difference, the overall SFR scales remain similar between the models. In the top right panel I show the evolution of cold gas mass in the disc. I define the radius of the disc as 10 kpc while the height of the disc as 4 kpc. The temperature threshold for separating cold gas and hot gas is 3×10^4K. Basically, the trends in this panel follow those of the SFR since star-forming gas is mainly of cold gas.

Mass outflow rate $\dot{M}_{\rm out}$ and energy outflow rate $\dot{E}_{\rm out}$ are also clear indicators of AGN feedback strength. Stronger AGN feedback will push more gas outward into ISM and potentially CGM scale with faster velocity. Here the outflow rate accounts only for gas particles with positive radial velocity within a shell locate at r and calculated by

$$\dot{M}_{\rm out}(r) = \frac{\Delta M(r)\langle v_r\rangle}{2\Delta r} \tag{4.1}$$

where $\Delta M(r)$ is the sum of the mass of all selected particles within the shell, $\langle v_r\rangle$ is mass weighted radial velocity of these particles, Δr is the half width of the shell. The energy outflow rate is therefore derived by $\dot{E}_{\rm out}(r) = \dot{M}_{\rm out}(r)\langle v_r\rangle^2/2$. In the second row, I show the mass outflow rate $\dot{M}_{\rm out,r=50kpc}$ and energy outflow rate $\dot{E}_{\rm out,r=50kpc}$ measured at 50kpc. As one can see that the results with low mass BHs are close to SN only run, indicating that the AGN feedback is insufficient to influence gas at such large radius. Instead, for high mass BH cases, they are clearly with higher $\dot{M}_{\rm out,r=50kpc}$ and $\dot{E}_{\rm out,r=50kpc}$, providing evidence of strong AGN feedback. When compare constant coupling efficiency model to fiducial variable coupling efficiency model, one can see that the latter yield smaller

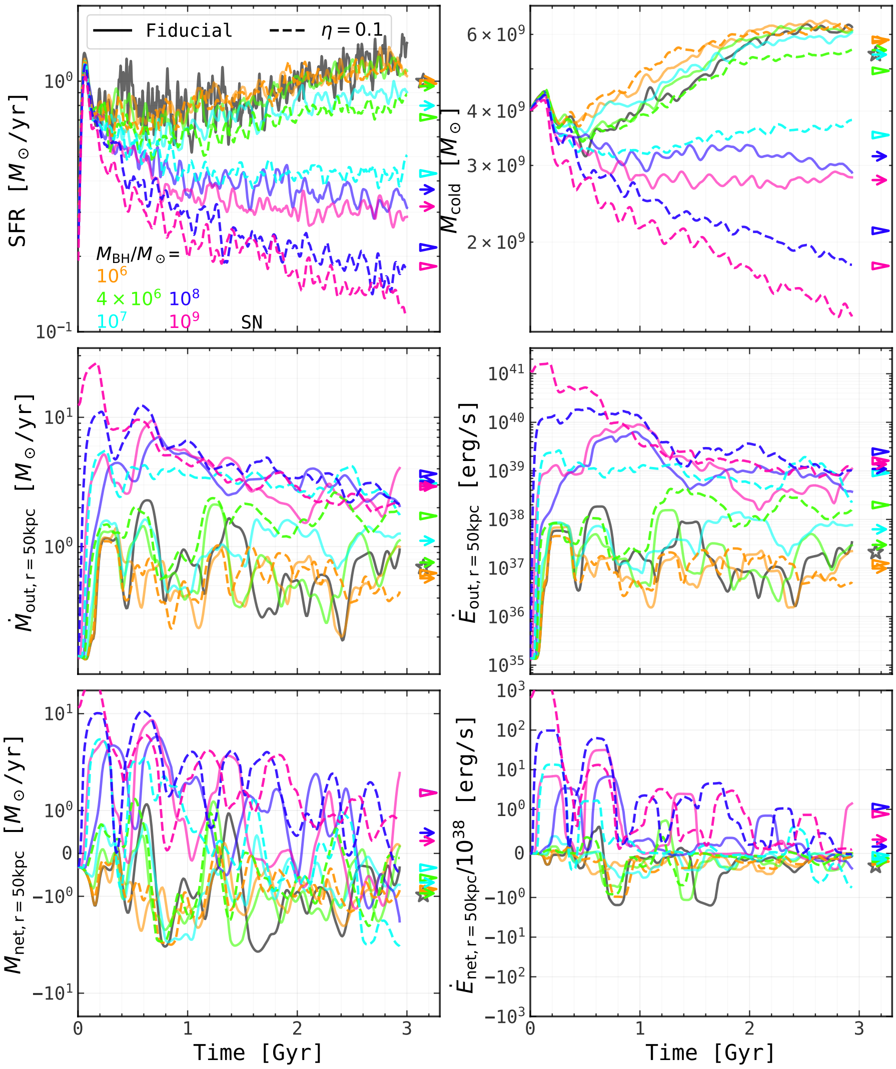

Figure 4.5: Galaxy property comparisons between fiducial variable coupling efficiency model and constant coupling efficiency model $\eta = 0.1$. Each panel shows a comparison in different galaxy properties including SFR, $M_{\rm cold}$, $\dot{M}_{\rm out,r=50kpc}$, $\dot{E}_{\rm out,r=50kpc}$, $\dot{M}_{\rm net,r=50kpc}$, $\dot{E}_{\rm net,r=50kpc}$. The black lines and corresponding mean values marked as star symbols represent SN only run. Everything else remain the same as Fig. 4.2. In the last row, I use symmetric logarithmic scale on y-axis and the threshold separating linear regime and logarithmic regime is 1. **This figure indicates that higher BH mass lead to smaller SFR and cold gas mass but higher mass outflow rate and energy outflow rate. Fiducial variable coupling efficiency model will less suppress SFR with higher cold gas mass, exhibit smaller mass outflow rate and energy outflow rate.**

$\dot{M}_{\rm out,r=50kpc}$ and $\dot{E}_{\rm out,r=50kpc}$ with the differences beging larger at the beginning of simulation for high mass BHs cases.

In the third row, I present net mass outflow rate $\dot{M}_{\rm net,r=50kpc}$ and net energy outflow rate $\dot{E}_{\rm net,r=50kpc}$. These metrics provide insights into the overall balance of gas inflow and outflow. "Galaxy fountain" can be seen when when these rates oscillate around zero, indicating alternating periods of inflow and outflow. For low mass BHs cases, both $\dot{M}_{\rm net,r=50kpc}$ and $\dot{E}_{\rm net,r=50kpc}$ keep below 0 for most of time while the high mass BHs cases keep above 0 for most of time, indicating that gas infall driven by gas cooling in CGM is dominant for low mass BH cases while gas outflow driven by AGN feedback is dominant for high mass BH cases, at this radius. The differences between the constant coupling efficiency model and the fiducial variable coupling efficiency model follow a similar trend to what is observed in the second row: the fiducial variable coupling efficiency model exhibits lower net outflow rates compared to the constant coupling efficiency model, with more pronounced differences in high-mass BH cases.

In Fig. 4.6, I test how variations in either the normalization N_η or slope α_η while keeping the other fixed will affect galaxy properties. In the first two rows, there is a evidence that lower α_η and higher N_η lead to more suppressed SFR smaller mass of cold gas disc. This can be explained by the energy differences shown in the first two row of Fig. 4.3. Interestingly, while low mass BH cases exhibit significant differences in energy output, these differences result in very small changes in SFR and $M_{\rm cold}$. Instead, the SFR and $M_{\rm cold}$ are nearly identical for $M_{\rm BH} = 10^6$ while the impact is more significant in high mass BH cases. This is because AGN feedback from low mass BHs is relatively weak while feedback from high-mass BHs plays a critical role in shaping galaxy properties, even when the energy differences are comparatively small. For $\dot{M}_{\rm out,r=50kpc}$ and $\dot{E}_{\rm out,r=50kpc}$, I find that lower α_η and higher N_η result in stronger outflow as $\dot{M}_{\rm out,r=50kpc}$ and $\dot{E}_{\rm out,r=50kpc}$ are closely connected to AGN feedback strength. However, the influence of BH masses on outflow when changing these two parameters is not monotonic. For $M_{\rm BH} = 10^6, 10^8 M_\odot$ cases, different models show very close results while the scatter is larger for $M_{\rm BH} = 10^7 M_\odot$ case. This may occur because $M_{\rm BH} = 10^6 M_\odot$ case produces feedback that is too weak to drive substantial outflows, while $M_{\rm BH} = 10^8 M_\odot$ case produce fewer feedback events, resulting in similar outflow behavior across parameter variations. When looking into $\dot{M}_{\rm net,r=50kpc}$ and $\dot{E}_{\rm net,r=50kpc}$, I find that gas infall is dominant for most of

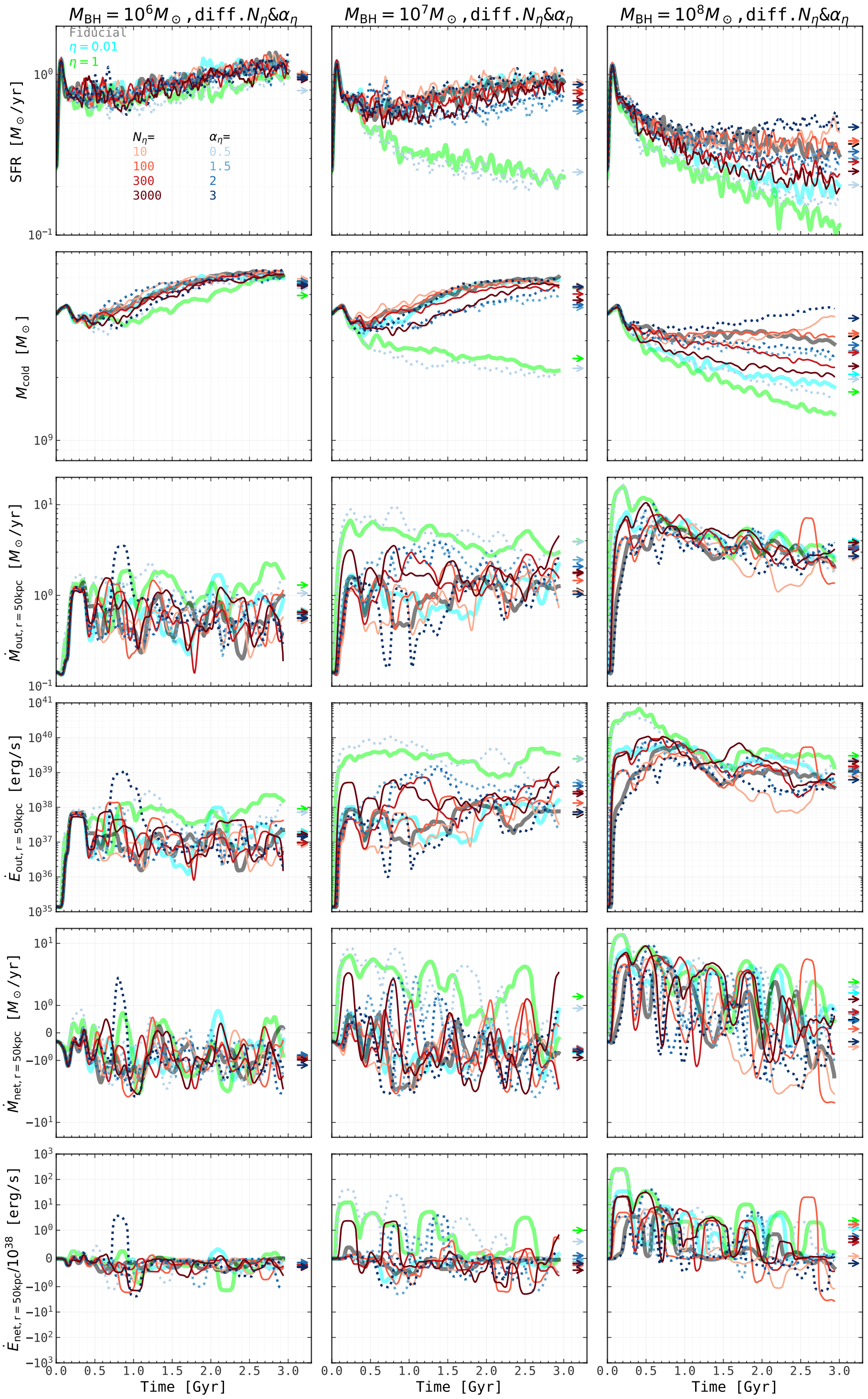

Figure 4.6: Galaxy property comparisons between variable coupling efficiency models varying normalization or slope while fixing the other. Each row shows a comparison in different feedback properties including SFR, $M_{\rm cold}$, $\dot{M}_{\rm out,r=50kpc}$, $\dot{E}_{\rm out,r=50kpc}$, $\dot{M}_{\rm net,r=50kpc}$, $\dot{E}_{\rm net,r=50kpc}$. Each column stand for a black hole mass. Everything else remain the same as Fig. 4.3. **This figure indicates that higher η (lower α_η or higher N_η) lead to smaller SFR and cold gas mass but higher mass outflow rate and energy rate. Additionally, from both net outflow rate and outflow rate, $M_{\rm BH} = 10^6 M_\odot$ cases are infall-dominant while $M_{\rm BH} = 10^8 M_\odot$ cases are outflow-dominant. For $M_{\rm BH} = 10^7 M_\odot$ cases, the stage can be transitioned from infall-dominant to outflow dominant with high η (lowα_η or high N_η).**

time in $M_{\rm BH} = 10^6 M_\odot$ cases, regardless of the parameters I varied. However, for $M_{\rm BH} = 10^7 M_\odot$ cases, the galaxy can transition from being gas infall-dominated to gas outflow-dominated if a smaller α_η is set, leading to stronger AGN feedback. For $M_{\rm BH} = 10^8 M_\odot$ cases, nearly all models show gas outflow dominant except some runs with small N_η, which correspond to weaker AGN feedback. These, again, confirm that BH mass is the zeroth-order factor influencing galaxy and AGN properties. If $M_{\rm BH}$ is too small, this model might not work efficiently.

Finally, I examine the influence on galaxy properties when using dependent N_η and α_η by $N_\eta = 39.81 \times 10^{\alpha_\eta - 2.6}$. For SFR and $M_{\rm cold}$, one can see that these parameter combinations cannot suppress star formation well in the $M_{\rm BH} = 10^6, 10^7 M_\odot$ cases while $M_{\rm BH} = 10^8 M_\odot$ can. Additionally, smaller α_η lead to lower SFR and $M_{\rm cold}$. These dependence can be interpreted by their corresponding AGN energy as shown in Fig. 4.4 where I show that lower values of α_η in this sampling method would lead to higher AGN energy. For $\dot{M}_{\rm out,r=50kpc}$ and $\dot{E}_{\rm out,r=50kpc}$, I also find that the scatter of $M_{\rm BH} = 10^6, 10^8 M_\odot$ cases are still smaller because of the same reason. When comparing $\dot{M}_{\rm net,r=50kpc}$ and $\dot{E}_{\rm net,r=50kpc}$ of $M_{\rm BH} = 10^6, 10^7 M_\odot$ cases, I find that these two properties are closer to zero compared other parameter combinations in Fig. 4.6, which means that the outflow and infall are more balanced while the $M_{\rm BH} = 10^8 M_\odot$ case is still dominated by outflow due to strong AGN feedback.

4.3 Convergence tests

In this section, I show the convergence tests for different runs. I mainly focus on the AGN energy measurements and BH mass measurements since they are directly correlated with AGN model including coupling efficiency. This section is necessary since it answer two questions: Are feedback properties accurately sampled? And how and why are certain settings, such as employing significantly smaller timesteps for BH calculations, chosen as fiducial? For BH mass, I use two measurement methods. The first method relies on the BH mass saved in the output files while the second calculates BH mass with accretion rate by $\Delta M_{\rm BH} = \int (1 - \epsilon_r) \dot{M} {\rm d}t$. For AGN energy, I have three measurement approaches. The first sums the energy saved in gas and star particles, as well as the energy reservoir, based on snapshot data. The second sums the energy injected by AGN saved in the BH particles and energy reservoir using snapshot data. In the

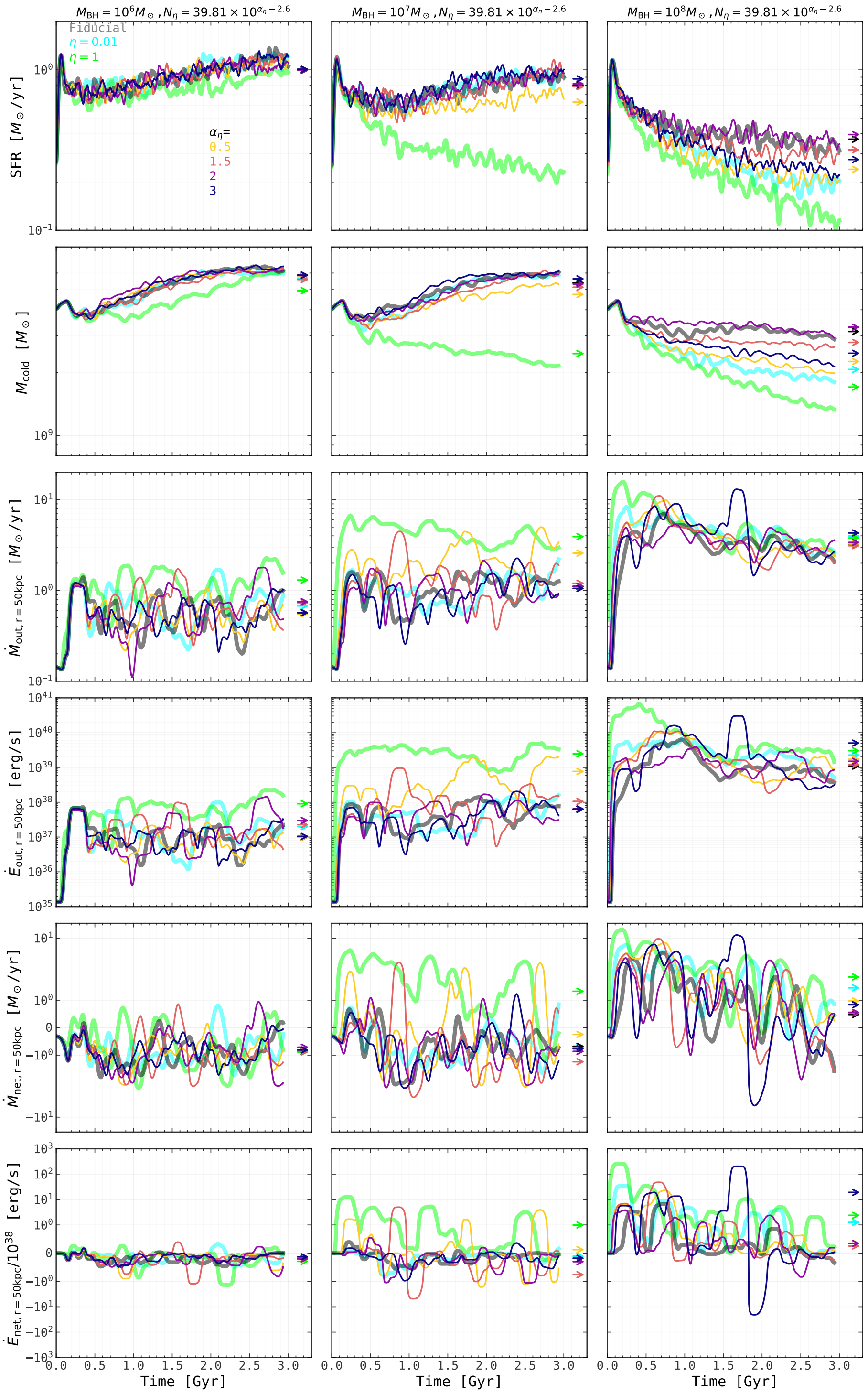

Figure 4.7: Similar to Fig. 4.7 but I show the comparison between variable coupling efficiency models varying normalization and slope following $N_\eta = 39.81 \times 10^{\alpha_\eta - 2.6}$. Everything else remain the same as Fig. 4.7. **This figure indicates that for dependent N_η and α_η, lower α_η lead to higher η, which result smaller SFR and cold gas mass but higher mass outflow rate and energy outflow rate.**

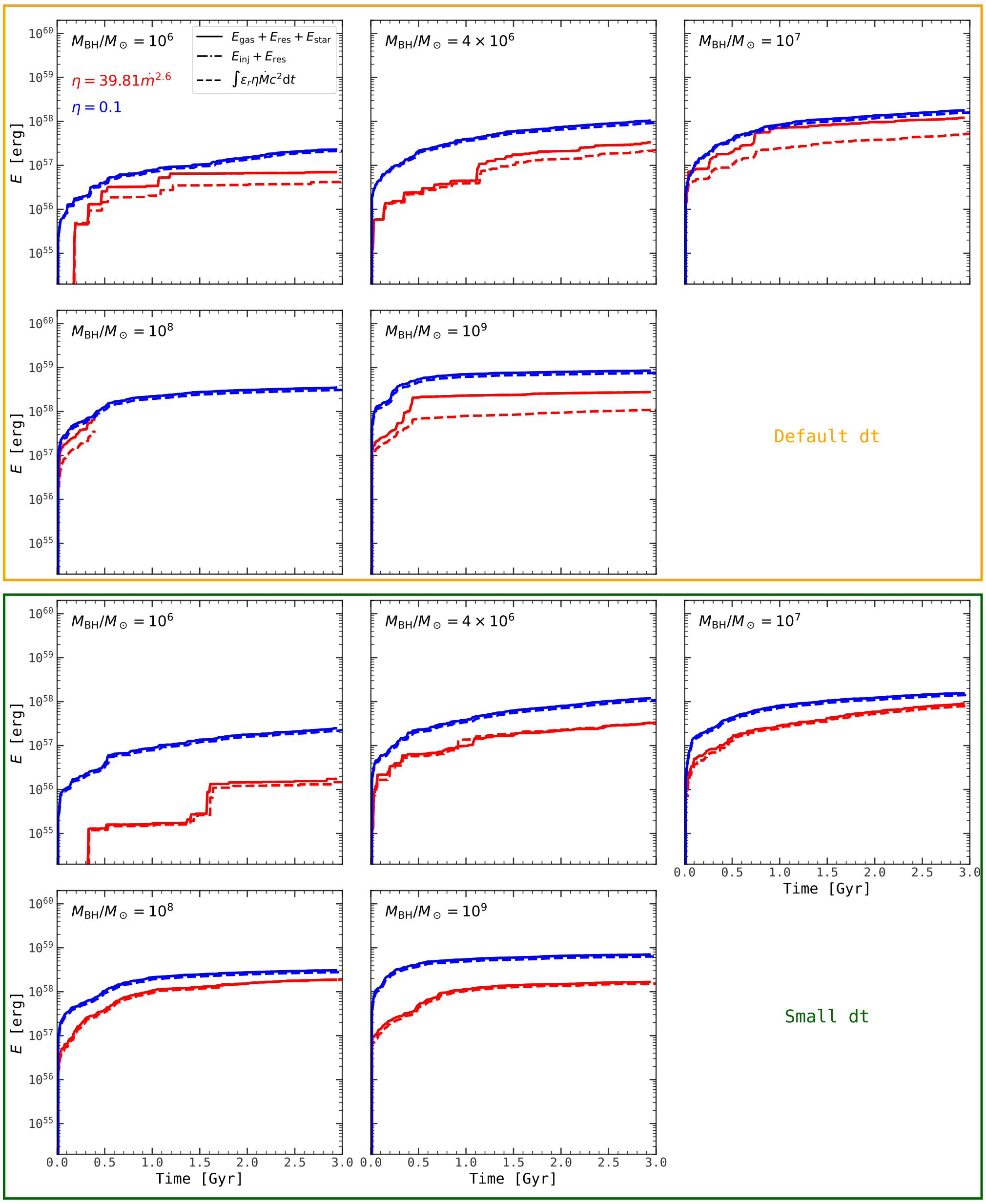

Figure 4.8: Convergence tests of AGN energies measured by different methods. In each panel, the blue lines represent runs with constant coupling efficiency ($\eta = 0.1$) while the red lines represent our variable coupling efficiency model using fiducial parameters ($N_\eta = 39.81$, $\alpha_\eta = 2.6$). The solid lines stand for the AGN energy computed as the sum of the energy retained by gas particles, star particles, and the energy reservoir. The dash-dotted lines stand for sum of the AGN energy injected and saved by BH particles and the energy reservoir, which are completely overlapped with solid lines. The dash lines represent the energy calculated by $\int \epsilon_r \eta \dot{M} c^2 \mathrm{d}t$. The first two rows show the results using default time step calculation in BH module. The last two rows show the result using much smaller time step calculation in BH module. Each panel stands for a BH mass as marked in the upper left of each panel ($M_{\mathrm{BH}}/M_\odot = 10^6, 4\times10^6, 10^7, 10^8, 10^9$). The red lines in the second row, first column stop because heating too much issue (see context). **This figure indicate that variable coupling efficiency model needs smaller time step to get converged in AGN energy**

third one, I calculate it by using $E = \int \epsilon_r \eta \dot{M} c^2 \mathrm{d}t$. In principle, the two mass measurements and three energy measurements should be consistent. However, some discrepancies might exist especially in energy measurements. Potential reasons include inaccuracies in calculating BH properties due to insufficiently small timesteps in BH calculations, or inaccuracies in integration results caused by output timesteps that are too large.

In Fig. 4.8, I present convergence tests for AGN energy in both constant coupling efficiency runs and variable coupling efficiency runs based on the fiducial parameters. Regardless of which timestep used, the constant coupling efficiency runs consistently show agreement across different energy measurements. This indicates that the default COLIBRE model yields convergence in AGN energy. However, in our variable coupling efficiency runs, discrepancies appear if I use default COLIBRE setting, i.e. using default timestep when calcuate BH properties. Furthermore, for variable coupling efficiency model, a numerical issue causes the simulation with $M_{\mathrm{BH}} = 10^8 M_{\odot}$ to stop around ~ 0.4 Gyr, as shown in the first panel of the second row. This issue occurs when a gas particle is overheated by multiple feedback events, likely due to an insufficiently small timestep. Therefore, based on this setting, I significantly reduce the BH timestep by modifying the timestep calculation (see Section 3.2), resulting in much closer agreement across energy measurements. The need for such small timesteps in the variable coupling efficiency model arises from wide dynamic range and frequent fluctuations in coupling efficiency. If timestep is not small enough, extreme high or low values may be missed, leading to discrepancies in the energy calculated through time integration compared to the other two methods. In addition, the measurements from the other two methods might be inaccurate as well.

When looking into convergence tests for BH mass increment in Fig. 4.9, I find that nearly all models with different BH masses can converge well. However, exceptions occur in high mass BH cases for the constant coupling efficiency model. The mass differences calculated by accretion rate are slightly higher than differences saved in the output. This discrepancy might be because the timestep in BH calculation are set to be too small for high mass BH cases (as the modified timestep is expressed as $\Delta t \propto 1/\dot{M}_{\mathrm{Edd}} \propto 1/M_{\mathrm{BH}}$, see Section 3.2). In that case, one needs smaller timestep for recording the output file to get convergence. This will significantly increasing the cost time and take up more storage. Given the small difference and our variation comparisons mainly focusing on

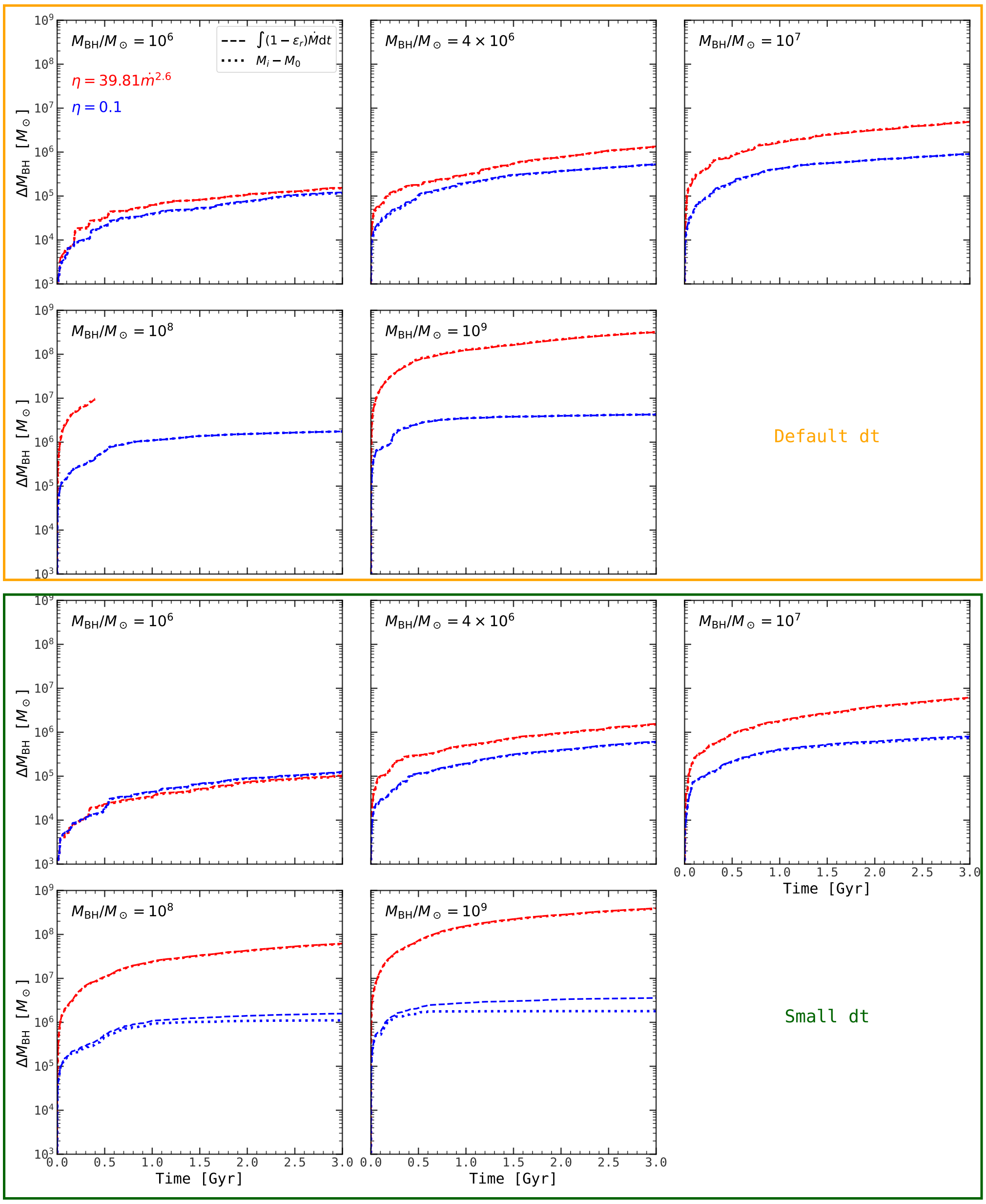

Figure 4.9: Convergence tests of BH mass increments measured by different methods. In each panel, the dash lines represent the mass difference computed by integration of accretion rate while the dotted lines represent the mass difference calculated by the recorded BH mass in the data outputs. Everything else remain the same as Fig. 4.8. **This figure indicate BH mass differences are consistent well with different measurements, regardless of which timestep is chosen. But smaller timestep in the output is needed if BH timestep is too small.**

$M_{\rm BH} = 10^6, 10^7, 10^8 M_\odot$ cases (e.g. Fig. 4.3), I adopt this setting as fiducial.

Since I have explored the parameter variations for our variable coupling efficiency model in this chapter before, it is necessary to assess convergence for these runs. In Fig. 4.10, I compare energy measurements for different normalization N_η and slope α_η that I used as well as for different BH masses that I explored. Using the fiducial setting (small BH timestep), I get nearly all runs converge in terms of AGN energy. The only exception is when I set $N_\eta = 100$ and $\alpha_\eta = 3$ for $M_{\rm BH} = 10^8 M_\odot$, as shown in bottom left panel. I check that that the inconsistency appears at the time when the corresponding $\eta = 1$ due to the ceiling (eq. (3.4)). Such large η values combined with corresponding $\dot{M}$ would need much smaller timestep in the outputs to achieve convergence, given that the BH timestep is small enough from other convergence tests. But the discrepancy is only ~ 0.2dex, which confirm that our fiducial settings remain reasonable and effective across the different runs. When examining their convergence in terms of BH mass difference in Fig. 4.11, I find that nearly all simulations get converged except high η cases ($N_\eta = 39.81$, $\alpha = 0.5$, see the fourth row in Fig. 4.3) for high mass BH cases ($M_{\rm BH} = 10^7, 10^8 M_\odot$). Similar discrepancies also exist in constant high η cases ($\eta = 1$), as shown in the first row of Fig. 4.12. These cases share similar high values of η. This indicate that higher values of η require smaller timestep for recording outputs. For other panels in Fig. 4.11 and Fig. 4.12, different measurements agree pretty well.

It is important to note that these discrepancies do not necessarily indicate inconsistency inside the simulation code. Instead, they arise might just because the timestep used for recording outputs is not small enough to do accurate integration over the output values.

4.4 Comparison with other AGN wind feedback model

In this section, I discuss the common features and differences between our models and previous works (Torrey et al., 2020; Costa et al., 2020), focusing on AGN wind feedback of idealised disc galaxies. Specifically, I compare the magnitude of SFR suppression and the associated timescales. Due to differences in subgrid physics and ICs across simulations, our analysis focuses on comparing the trends in SFR and their relation with AGN feedback strength.

In Torrey et al. (2020), the authors implement a scheme for feedback from

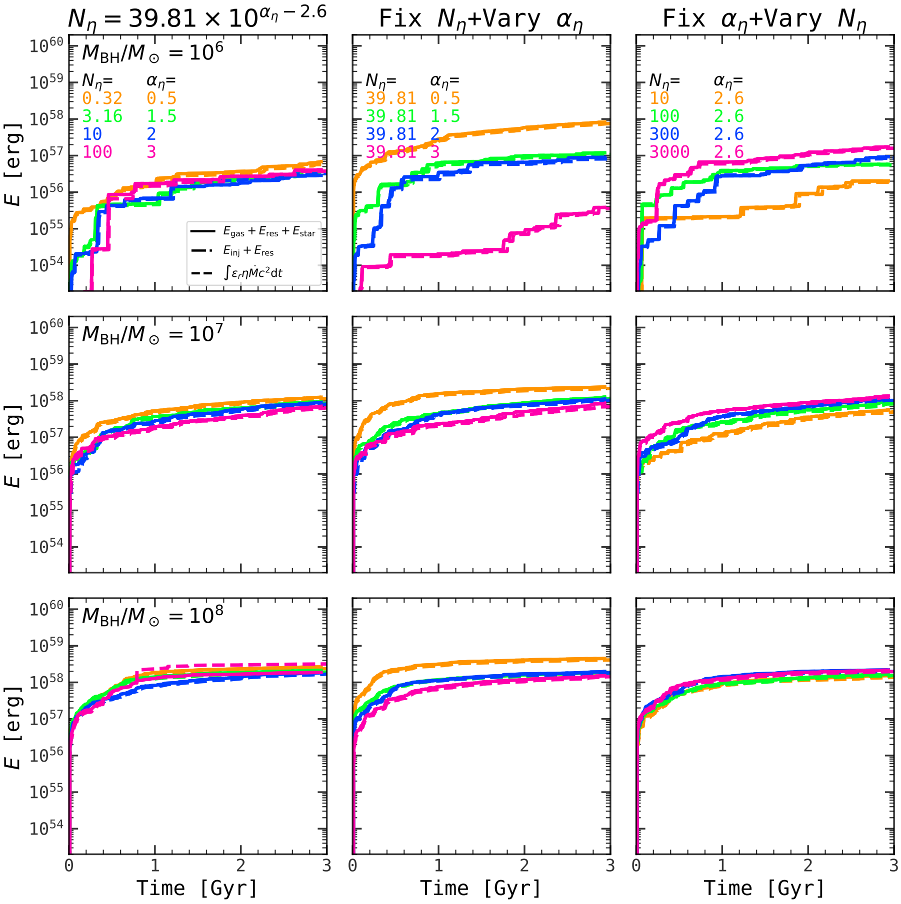

Figure 4.10: Convergence tests of AGN energies measured by different methods for variable coupling efficiency model with different values beyond fiducial model. The linestyle remain the same as Fig. 4.8. Each row stands for a BH mass ($M_{\rm BH}/M_\odot = 10^6, 10^7, 10^8$). The first column show the results with variation using $N_\eta = 39.81 \times 10^{\alpha_\eta} - 2.6$. In the second and third column, I vary either the N_η or the α_η while keeping the other fixed. The exact values of N_η and α_η as well as their presented color are show in the upper left and upper middle panels. All runs are using small BH timestep. **This figure prove that nearly all runs with different N_η and α_η show convergence for different energy measurements except very high η runs.**

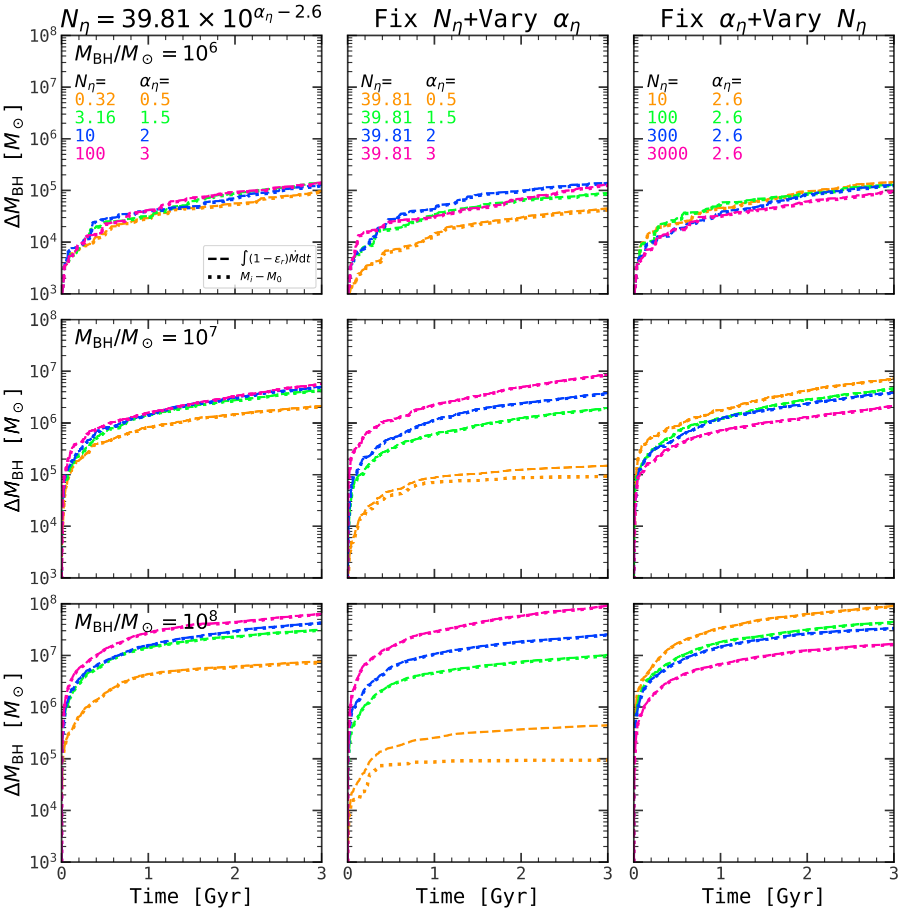

Figure 4.11: Convergence tests of BH mass increments measured by different methods for variable coupling efficiency model with different values beyond fiducial model. The linestyle remain the same as Fig. 4.9. Everything else remain the same Fig. 4.10. **This figure prove that nearly all runs with different N_η and α_η show convergence for different mass measurements except very high η runs.**

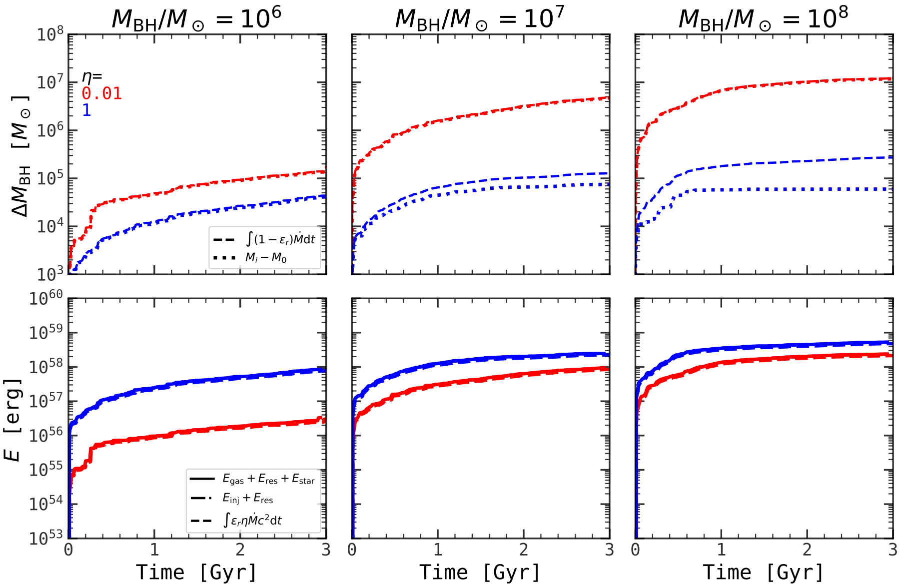

Figure 4.12: Convergence tests of BH mass increments (first row) or AGN energies (second row) measured by different methods for constant coupling efficiency models with higher value ($\eta = 1$, blue) or lower value ($\eta = 0.01$, red). The linestyle of the first row remain the same as Fig. 4.9 while the linestyle of the second row remain the same as Fig. 4.8. **This figure prove that nearly all runs with different η show convergence for different energy measurements except very high η runs.**

BAL winds and examine their impact in simulations of isolated disc galaxies, spanning from from MW-mass to high mass disc galaxies, using `GIZMO` hydrodynamical code (Hopkins, 2017) and FIRE subgrid physics model (Hopkins et al., 2018) with turning on cooling, star formation and SN feedback. Their ICs contain gas discs, stellar discs, stellar bulges, central SMBHs, and live dark matter halos, but exclude a CGM. The mass resolution is $2-5\times10^3 M_\odot$, significantly higher than ours. In their simulations, the BH accretion rate is fixed as the Eddington accretion rate and BAL wind mass launching rate is defined by $\dot{M}_{\rm BAL}\eta_{\rm BAL}$. AGN feedback in their model is implemented as isotropic kinetic feedback. The AGN energy rate is modeled by $\dot{E}_{\rm BAL}=\eta_{\rm BAL}\dot{M}v_{\rm BAL}^2/2$. Here the $\eta_{\rm BAL}$ and $v_{\rm BAL}$ are BAL wind mass loading and BAL wind speed, which are free parameters. This approach differs from our energy rate ($\dot{E}_{\rm AGN}=\epsilon_r\eta\dot{M}c^2$). Using their fiducial value ($\eta_{\rm BAL}=1$ and $v_{\rm BAL}=0.1c$), the energy rate in their model is $5\times10^{-2}/\eta$ times ours for the same accretion rate and $\epsilon_r=0.1$. This implies that their energy rate is half of ours when assuming our default constant coupling efficiency ($\eta=0.1$) or $\sim 6.25-25$ times higher than ours when using fiducial variable coupling efficiency model. Since they fix the accretion rate as Eddington rate, their feedback energy is further amplified. Although the ICs of their isolated disky galaxies are different from ours, I compare the SFR in our $M_{\rm BH}=10^8, 10^9 M_\odot$ cases using both default constant coupling efficiency model and fiducial variable coupling efficiency model with their **G4** run with the same BH mass (Figure 6, Torrey et al., 2020). This run has a similar total disc mass ($6.2\times10^{10}M_\odot$) but a higher cold gas disc fraction (20%).

G4 exhibits a peak SFR$\sim 5M_\odot$/yr at $\sim$ 10 Myr and drop to SFR$\sim 3M_\odot$/yr (0.2 dex) for $M_{\rm BH}=10^8M_\odot$ case at 50 Myrs and drop below 0.6 $M_\odot$/yr (0.9 dex) for $M_{\rm BH}=10^9M_\odot$ case. This fast suppression indicates strong AGN feedback. For our runs, all models have a peak SFR$\sim 1M_\odot$/yr at $\sim$ 50 Myr. The constant coupling efficiency model drops to SFR$\sim 0.2-0.3M_\odot$/yr (0.7-0.8 dex) while the fiducial variable coupling efficiency model drops to SFR$\sim 0.35M_\odot$/yr (0.65 dex). Different from their results, our simulations do not exhibit significant differences between the $M_{\rm BH}=10^8M_\odot$ and $M_{\rm BH}=10^9M_\odot$ cases. Presumably this is because in ours sims, the BH accretion rate is calculated self-consistently from the Bondi-Hoyle formula, rather than being assumed fixed. This allows the BH accretion rate to self-regulate in our sims, which is not possible in theirs. For both default constant coupling efficiency model and fiducial variable coupling efficiency model, they show larger relative difference in $M_{\rm BH}=10^8M_\odot$ case (0.65-0.8 dex compared to their 0.2 dex) but smaller relative difference in $M_{\rm BH} = 10^9 M_\odot$ case (0.65-0.8 dex compared to their 0.8 dex), compared to the relative different in their results. Furthermore, our results indicate a longer timescale for SFR suppression. The differences in SFR level could be due to different set up, e.g. cold gas disc fraction while the faster drop in their simulations could be attributed to stronger kinetic feedback. In their Figure 9 and Figure 10, they show that more energetic winds lead to larger momentum values in the outflows compared to wind momentum. Similarly, I show that energetic winds lead to larger energy rate values in the outflows for both default constant coupling efficiency model and fiducial variable coupling efficiency model in Fig. 4.5. However, this result is not unique and can be achieved in most simulations.

In Costa et al. (2020), the authors implement a new AGN kinetic feedback model through small-scale, ultrafast winds in the moving mesh hydrodynamic code `AREPO` (Weinberger et al., 2020). Different from ours, in their idealized simulations, they initialize a spinning spherical gas cloud by the same density profile of the DM halo without requiring dynamical equilibrium. They turn off SN feedback but include cooling and star formation. As a result, the spinning gas cloud collapses towards the centre of the halo, where it settles into a gas disc. And the rest of the spherical gas cloud can be treated as a CGM, without requiring dynamical equilibrium. Note that they don't directly initialize stellar disc and CGM. The mass resolution for their fiducial runs is $1.6 \times 10^5 M_\odot$, comparable to ours. For SMBH, they initial their AGN bolometric luminosity ($10^{45} - 5 \times 10^{47}$ erg/s) instead of $M_{\rm BH}$, and fix the AGN bolometric luminosity during the evolution. Given our $\dot{m}$ is starting from $\sim 10^{-2}$ for both default constant coupling efficiency model and fiducial variable coupling efficiency model, the corresponding initial $M_{\rm BH}$ is $\sim 8 \times 10^8 - 4 \times 10^{11} M_\odot$. Therefore, I choose $M_{\rm BH} = 10^9$ in our both models to make comparisons with their $L_{\rm bol} = 10^{45} M_\odot$ case. In their feedback model, they parametrize the AGN energy input by $\dot{E}_{\rm w} = \tau \beta \epsilon_r \dot{M} c^2/2$, where τ and β are free parameters. In their work, τ is set as 1 and β is varying from 0.005 to 0.5, result in a factor of $\beta/(2\eta)$ difference compared to our AGN energy rate given the same BH mass. For default constant coupling efficiency model, this corresponds to a difference of 0.025-2.5. For our fiducial variable coupling efficiency model, the AGN energy input in their simulations could be 5–500 times higher than ours.

When compare SFR in $M_{\rm BH} = 10^9 M_\odot$ case with their $L_{\rm bol} = 10^{45} M_\odot$ case

(Figure 10, Costa et al., 2020), I find their results show that SFR reach maximum at about 0.1 Gyr before declining, whereas the timescale for the peak in our models is around 0.05 Gyr. For their run with $L_{\rm bol} = 10^{45} L_\odot$, the SFR peaks at about 80 $M_\odot$/yr and drop to $\sim 35 M_\odot$/yr (a drop of $\sim 56.25\%$, similar to their no AGN run, assuming $\beta = 0.017$) or $\sim 10 M_\odot$/yr (a drop of $\sim 87.5\%$, assuming $\beta = 0.1$) after 0.5 Gyr. In contrast, our result with $M_{\rm BH} = 10^9 M_\odot$ change from $1 M_\odot$/yr to $\sim 0.3 M_\odot$/yr (a $\sim 70\%$ drop, default constant coupling efficiency model) or $\sim 0.5 M_\odot$/yr (a $\sim 50\%$ drop, fiducial variable coupling efficiency model), given the same time. The different peak values of SFR could be because different ICs, e.g. gas content, or different subgrid physics model, e.g. cooling. Notably, they assume an initial spherical gas fraction as 0.17. If the cooling is very strong, this potentially lead to much higher cold gas-to-total mass ratio compared to ours (0.036), which result in much higher SFR peak. When compare their $\beta = 0.017$ case and $\beta = 0.1$ case with our default constant coupling efficiency, one can find $\beta/(2\eta)$ is actually smaller than unity. If the bolometric luminosity or accretion rate are the same, our results will result in higher AGN energy input and suppress SFR with higher relative difference. However, the relative different in SFR for our default constant coupling efficiency model only slight larger than their $\beta = 0.017$ case but smaller than their $\beta = 0.1$ case, suggesting stronger kinetic AGN feedback potentially due to fast declining of accretion rate for our default constant coupling efficiency model. When comparing our fiducial variable coupling efficiency case, I find that the relative different in SFR is smaller than both their cases potentially due smaller η resulting in large $\beta/(2\eta)$ values. The common thing is that when changing parameters, strong feedback or higher AGN energy input would lead to lower SFR while weaker feedback or lower AGN energy input would brings the SFR closer to the no AGN runs. (see comparison between fiducial variable coupling efficiency models and default constant coupling efficiency models in Fig. 4.5).

In short, although different simulations lead to different SFR peaks, quenching timescale, and the exact values of SFR at final time due to different ICs and subgrid physics model, both of them show that parameters that lead to strong AGN feedback will result in lower SFR, consistent with our results.

Chapter 5

Conclusion

In this thesis, I go over the physical mechanism of UV line driven winds, introduce and improve the simplified model Qwind (Quera-Bofarull et al., 2023). After comparing the scaling relation in terms of $\dot{M}_{\rm wind}/\dot{M}$, $L_{\rm kin}/L_{\rm bol}$, $\dot{p}_{\rm wind}/(L_{\rm bol}/c)$, $\langle v_r \rangle/c$ between observation (Mestici et al., 2024), Qwind model (Quera-Bofarull et al., 2023), and RHD simulation (Nomura & Ohsuga, 2017), I build up a relation connecting coupling efficiency and Eddington ratio: $\eta = N_\eta \dot{m}^{\alpha_\eta}$. I then implement this into hydrodynamical cosmological code `SWIFT` (Schaller et al., 2024) and run a series of idealized MW-like galaxies with COLIBRE subgrid physics model (Schaye et al., in prep.). I initialize a static DM halo, a cold gas disc, a stellar disc and a hot CGM in equilibrium using methods from Nobels et al. (2022, 2024), with some updates. Gas cooling, star formation and SN feedback are included. Gas is assumed to accrete onto the BH at a rate given by the Bondi-Hoyle formula. I vary black hole mass ($M_{\rm BH} = 10^6, 4 \times 10^6, 10^7, 10^8, 10^9 M_\odot$), normalization and slopes in coupling efficiency to explore the influence of this model on feedback properties and galaxy properties. I then compare our results with previous simulation work focusing on AGN wind feedback in idealized disky galaxies (Torrey et al., 2020; Costa et al., 2020). I also show convergence tests for our runs to confirm the result can be trusted and illustrate how I determine some settings as fiducial. The main conclusions for this model are summarized below:

1. BH mass is the zeroth-order quantity governs different feedback and galaxy properties. Specifically, higher BH mass will lead to higher cumulative AGN energy and AGN energy rate when the feedback model parameters are kept fixed, due to higher BH masses leading to higher BH accretion rates. This will suppress star formation, lead to smaller cold gas mass, result in higher

gas mass outflow rate and energy outflow rate.

2. When comparing fiducial variable coupling efficiency models ($N_\eta = 39.81$, $\alpha_\eta = 2.6$) with default constant coupling efficiency models ($\eta = 0.1$), I find that for a given black hole mass, the former one generate less AGN energy due to generally lower coupling efficiency, suppress less on SFR, $M_{\rm cold}$, produce weaker outflow, lead to faster BH growth.

3. The systematics of normalization and slope are connected to their corresponding coupling efficiency. For both varying methods, i.e. sample N_η and α_η independently or dependently requiring $\eta = 0.1$ when $\dot{m} = 0.1$, higher normalization or lower slope increase typical coupling efficiency, typically resulting in higher AGN energy and energy rate, although the differences become small especially for high mass BH cases due to self-regulation. However, even small differences in AGN energy will exhibit significant impact on galaxy properties. Specifically, higher normalization or lower slope yield smaller SFR and $M_{\rm cold}$, higher mass outflow rate and energy outflow rate, slower BH growth.

4. Compared to previous idealized disky galaxy simulations, our results exhibit weaker AGN feedback and correspondingly less suppression of SFR. This could be because different ICs and subgrid models. More importantly, this might because our simulations calculate the BH accretion rate self-consistently, allowing the AGN feedback to self-regulate However, I show similar systematics with previous simulations in SFR. Specifically, stronger AGN feedback, controlled by larger coefficients in front of the AGN bolometric luminosity, leads to greater suppression of SFR for a given AGN bolometric luminosity or BH accretion rate.

5. Using a variable coupling efficiency model with different parameters enhances self-regulation in feedback properties depends on BH mass. For example, compared to default constant coupling efficiency cases, variable coupling efficiency cases show similar cumulative AGN energy or AGN energy injection rate as BH mass increasing. This potentially due to compensation between coupling efficiency and the BH accretion rate.

6. To achieve convergence of mass accreted onto BH and AGN energy injected and avoid overheating issue, the timestep of BH calculation should be set much smaller than default calculation in COLIBRE. However, smaller

timestep in BH calculation would require smaller timestep in the output to achieve convergence in different energy and mass measurements, especially for high η cases and high mass BH cases.

Note that these conclusions are based on idealized MW-like galaxies and might be sensitive to the initial conditon that I set. The model performance may differ in cosmological simulations or in idealized elliptical galaxies. But one might expect that implementing this model into cosmological simulations without changing any other subgrid model parameters will lead to higher BH mass functions and stellar mass function for MW-mass like galaxies due to faster growth of BHs and higher SFR as shown before. This could potentially explain the existence of some massive galaxies or SMBH at very high redshift in the JWST era. Note that if the fast BH growth happens for z=0, the results would conflict with observations. Therefore, one might need a additional model to transition the coupling efficiency to the default constant value as redshift decreasing, which lead to faster BH growth at high-z, but the same total growth by $z = 0$.

As for the model itself, while the fiducial normalization in the varying coupling efficiency model is motivated by observation (Mestici et al., 2024) and the fiducial slope is motivated by Qwind (Quera-Bofarull et al., 2023), the variations of normalizations and slopes are somewhat arbitrary. To constrain this better, one might need more accurate observational data. It is worth considering that normalization and slope might not be constants but instead functions of black hole properties, such as mass and spin. Incorporating such dependencies would require the development of a more sophisticated AGN feedback model. All of these are left for future studies.

Bibliography

Abramowicz M. A., Czerny B., Lasota J. P., Szuszkiewicz E., 1988, Astrophysical Journal, 332, 646

Bahé Y. M., et al., 2022, Monthly Notices of the Royal Astronomical Society, 516, 167

Behroozi P., Wechsler R. H., Hearin A. P., Conroy C., 2019, Monthly Notices of the Royal Astronomical Society, 488, 3143

Bird S., Ni Y., Di Matteo T., Croft R., Feng Y., Chen N., 2022, Monthly Notices of the Royal Astronomical Society, 512, 3703

Blandford R. D., Znajek R. L., 1977, Monthly Notices of the Royal Astronomical Society, 179, 433

Bondi H., Hoyle F., 1944, Monthly Notices of the Royal Astronomical Society, 104, 273

Booth C. M., Schaye J., 2009, Monthly Notices of the Royal Astronomical Society, 398, 53

Borrow J., Schaller M., Bower R. G., Schaye J., 2022, Monthly Notices of the Royal Astronomical Society, 511, 2367

Bower R. G., Benson A. J., Malbon R., Helly J. C., Frenk C. S., Baugh C. M., Cole S., Lacey C. G., 2006, Monthly Notices of the Royal Astronomical Society, 370, 645

Bullock J. S., Dekel A., Kolatt T. S., Kravtsov A. V., Klypin A. A., Porciani C., Primack J. R., 2001, Astrophysical Journal, 555, 240

Castor J. I., Abbott D. C., Klein R. I., 1975, Astrophysical Journal, 195, 157

Chaikin E., Schaye J., Schaller M., Benítez-Llambay A., Nobels F. S. J., Ploeckinger S., 2023, Monthly Notices of the Royal Astronomical Society, 523, 3709

Chartas G., et al., 2009, New Astronomy Reviews, 53, 128

Costa T., Sijacki D., Haehnelt M. G., 2014, Monthly Notices of the Royal Astronomical Society, 444, 2355

Costa T., Pakmor R., Springel V., 2020, Monthly Notices of the Royal Astronomical Society, 497, 5229

Davé R., Anglés-Alcázar D., Narayanan D., Li Q., Rafieferantsoa M. H., Appleby S., 2019, Monthly Notices of the Royal Astronomical Society, 486, 2827

Davis S. W., Laor A., 2011, Astrophysical Journal, 728, 98

Di Matteo T., Springel V., Hernquist L., 2005, Nature, 433, 604

Dittmann A. J., Cantiello M., 2024, arXiv e-prints, p. arXiv:2409.02981

Donnari M., Pillepich A., Nelson D., Marinacci F., Vogelsberger M., Hernquist L., 2021, Monthly Notices of the Royal Astronomical Society, 506, 4760

Dubois Y., et al., 2021, Astronomy and Astrophysics, 651, A109

Eldridge J. J., Stanway E. R., Xiao L., McClelland L. A. S., Taylor G., Ng M., Greis S. M. L., Bray J. C., 2017, Publications of the Astronomical Society of Australia, 34, e058

Event Horizon Telescope Collaboration et al., 2022, The Astrophysical Journal Letters, 930, L15

Fabian A. C., 2012, Annual Review of Astronomy & Astrophysics, 50, 455

Ferland G. J., et al., 2017, Revista Mexicana de Astronomía y Astrofísica, 53, 385

Fiore F., et al., 2017, Astronomy and Astrophysics, 601, A143

Gladstone J. C., Roberts T. P., Done C., 2009, Monthly Notices of the Royal Astronomical Society, 397, 1836

Gofford J., Reeves J. N., McLaughlin D. E., Braito V., Turner T. J., Tombesi F., Cappi M., 2015, Monthly Notices of the Royal Astronomical Society, 451, 4169

Greengard L., Rokhlin V., 1987, Journal of Computational Physics, 73, 325

Hagen S., Done C., 2023, Monthly Notices of the Royal Astronomical Society, 525, 3455

Harrison C. M., 2017, Nature Astronomy, 1, 0165

Harrison C. M., Ramos Almeida C., 2024, Galaxies, 12, 17

Henriques B. M. B., Yates R. M., Fu J., Guo Q., Kauffmann G., Srisawat C., Thomas P. A., White S. D. M., 2020, Monthly Notices of the Royal Astronomical Society, 491, 5795

Hernquist L., 1990, Astrophysical Journal, 356, 359

Higginbottom N., Proga D., Knigge C., Long K. S., Matthews J. H., Sim S. A., 2014, Astrophysical Journal, 789, 19

Higginbottom N., Scepi N., Knigge C., Long K. S., Matthews J. H., Sim S. A., 2024, Monthly Notices of the Royal Astronomical Society, 527, 9236

Hirschmann M., Dolag K., Saro A., Bachmann L., Borgani S., Burkert A., 2014, Monthly Notices of the Royal Astronomical Society, 442, 2304

Hopkins P. F., 2017, arXiv e-prints, p. arXiv:1712.01294

Hopkins P. F., Hernquist L., Cox T. J., Kereš D., 2008, The Astrophysical Journal Supplement Series, 175, 356

Hopkins P. F., et al., 2018, Monthly Notices of the Royal Astronomical Society, 480, 800

Hoyle F., Lyttleton R. A., 1939, Proceedings of the Cambridge Philosophical Society, 35, 405

Huško F., Lacey C. G., 2023a, Monthly Notices of the Royal Astronomical Society, 520, 5090

Huško F., Lacey C. G., 2023b, Monthly Notices of the Royal Astronomical Society, 521, 4375

Huško F., Lacey C. G., Roper W. J., Schaye J., Briggs J. M., Schaller M., 2024, arXiv e-prints, p. arXiv:2410.09450

Ishibashi W., Fabian A. C., Canning R. E. A., 2013, Monthly Notices of the Royal Astronomical Society, 431, 2350

Jiang Y.-F., Stone J. M., Davis S. W., 2014, Astrophysical Journal, 796, 106

Jiang Y.-F., Stone J. M., Davis S. W., 2019, Astrophysical Journal, 880, 67

Kaviraj S., et al., 2017, Monthly Notices of the Royal Astronomical Society, 467, 4739

King A., 2003, The Astrophysical Journal Letters, 596, L27

King A., 2005, The Astrophysical Journal Letters, 635, L121

King A., Pounds K., 2015, Annual Review of Astronomy & Astrophysics, 53, 115

King A. R., Zubovas K., Power C., 2011, Monthly Notices of the Royal Astronomical Society, 415, L6

Kormendy J., Ho L. C., 2013, Annual Review of Astronomy & Astrophysics, 51, 511

Koudmani S., Somerville R. S., Sijacki D., Bourne M. A., Jiang Y.-F., Profit K., 2024, Monthly Notices of the Royal Astronomical Society, 532, 60

Kubota A., Done C., 2018, Monthly Notices of the Royal Astronomical Society, 480, 1247

Lacey C. G., et al., 2016, Monthly Notices of the Royal Astronomical Society, 462, 3854

Lanzuisi G., Giustini M., Cappi M., Dadina M., Malaguti G., Vignali C., Chartas G., 2012, Astronomy and Astrophysics, 544, A2

Le Brun A. M. C., McCarthy I. G., Schaye J., Ponman T. J., 2014, Monthly Notices of the Royal Astronomical Society, 441, 1270

Luo B., et al., 2013, Astrophysical Journal, 772, 153

Marinacci F., et al., 2018, Monthly Notices of the Royal Astronomical Society, 480, 5113

McCarthy I. G., et al., 2010, Monthly Notices of the Royal Astronomical Society, 406, 822

McCarthy I. G., Schaye J., Bower R. G., Ponman T. J., Booth C. M., Dalla Vecchia C., Springel V., 2011, Monthly Notices of the Royal Astronomical Society, 412, 1965

McKinney J. C., Tchekhovskoy A., Blandford R. D., 2012, Monthly Notices of the Royal Astronomical Society, 423, 3083

McKinney J. C., Tchekhovskoy A., Sadowski A., Narayan R., 2014, Monthly Notices of the Royal Astronomical Society, 441, 3177

McNamara B. R., Nulsen P. E. J., 2007, Annual Review of Astronomy & Astrophysics, 45, 117

McNamara B. R., Nulsen P. E. J., Wise M. W., Rafferty D. A., Carilli C., Sarazin C. L., Blanton E. L., 2005, Nature, 433, 45

Mestici S., Tombesi F., Gaspari M., Piconcelli E., Panessa F., 2024, Monthly Notices of the Royal Astronomical Society, 532, 3036

Mo H. J., Mao S., White S. D. M., 1998, Monthly Notices of the Royal Astronomical Society, 295, 319

Monaghan J. J., 1992, Annual Review of Astronomy & Astrophysics, 30, 543

Murray N., Chiang J., Grossman S. A., Voit G. M., 1995, Astrophysical Journal, 451, 498

Narayan R., Yi I., 1994, The Astrophysical Journal Letters, 428, L13

Narayan R., SÄ dowski A., Penna R. F., Kulkarni A. K., 2012, Monthly Notices of the Royal Astronomical Society, 426, 3241

Navarro J. F., Frenk C. S., White S. D. M., 1997, Astrophysical Journal, 490, 493

Nelson D., et al., 2018, Monthly Notices of the Royal Astronomical Society, 475, 624

Nobels F. S. J., Schaye J., Schaller M., Bahé Y. M., Chaikin E., 2022, Monthly Notices of the Royal Astronomical Society, 515, 4838

Nobels F. S. J., Schaye J., Schaller M., Ploeckinger S., Chaikin E., Richings A. J., 2024, Monthly Notices of the Royal Astronomical Society, 532, 3299

Nomura M., Ohsuga K., 2017, Monthly Notices of the Royal Astronomical Society, 465, 2873

Nomura M., Ohsuga K., Takahashi H. R., Wada K., Yoshida T., 2016, Publications of the Astronomical Society of Japan, 68, 16

Novikov I. D., Thorne K. S., 1973, in Dewitt C., Dewitt B. S., eds, Black Holes (Les Astres Occlus). pp 343–450

Pillepich A., et al., 2018, Monthly Notices of the Royal Astronomical Society, 475, 648

Ploeckinger S., Schaye J., 2020, Monthly Notices of the Royal Astronomical Society, 497, 4857

Proga D., Stone J. M., Drew J. E., 1998, Monthly Notices of the Royal Astronomical Society, 295, 595

Proga D., Stone J. M., Kallman T. R., 2000, Astrophysical Journal, 543, 686

Quera-Bofarull A., Done C., Lacey C., McDowell J. C., Risaliti G., Elvis M., 2020, Monthly Notices of the Royal Astronomical Society, 495, 402

Quera-Bofarull A., Done C., Lacey C. G., Nomura M., Ohsuga K., 2023, Monthly Notices of the Royal Astronomical Society, 518, 2693

Richings A. J., Schaye J., Oppenheimer B. D., 2014a, Monthly Notices of the Royal Astronomical Society, 440, 3349

Richings A. J., Schaye J., Oppenheimer B. D., 2014b, Monthly Notices of the Royal Astronomical Society, 442, 2780

Richings A. J., Faucher-Giguère C.-A., Gurvich A. B., Schaye J., Hayward C. C., 2022, Monthly Notices of the Royal Astronomical Society, 517, 1557

Risaliti G., Elvis M., 2010, Astronomy and Astrophysics, 516, A89

Schaller M., et al., 2024, Monthly Notices of the Royal Astronomical Society, 530, 2378

Schaye J., et al., 2010, Monthly Notices of the Royal Astronomical Society, 402, 1536

Schaye J., et al., 2015, Monthly Notices of the Royal Astronomical Society, 446, 521

Shakura N. I., Sunyaev R. A., 1973, Astronomy and Astrophysics, 24, 337

Sijacki D., Springel V., 2006, Monthly Notices of the Royal Astronomical Society, 366, 397

Sijacki D., Vogelsberger M., Genel S., Springel V., Torrey P., Snyder G. F., Nelson D., Hernquist L., 2015, Monthly Notices of the Royal Astronomical Society, 452, 575

Silk J., 2005, Monthly Notices of the Royal Astronomical Society, 364, 1337

Silk J., 2013, Astrophysical Journal, 772, 112

Silk J., Begelman M. C., Norman C., Nusser A., Wyse R. F. G., 2024, The Astrophysical Journal Letters, 961, L39

Springel V., Di Matteo T., Hernquist L., 2005, Monthly Notices of the Royal Astronomical Society, 361, 776

Springel V., et al., 2018, Monthly Notices of the Royal Astronomical Society, 475, 676

Spruit H. C., Uzdensky D. A., 2005, Astrophysical Journal, 629, 960

Stanway E. R., Eldridge J. J., 2018, Monthly Notices of the Royal Astronomical Society, 479, 75

Stevens I. R., Kallman T. R., 1990, Astrophysical Journal, 365, 321

Tombesi F., Cappi M., Reeves J. N., Palumbo G. G. C., Yaqoob T., Braito V., Dadina M., 2010a, Astronomy and Astrophysics, 521, A57

Tombesi F., Sambruna R. M., Reeves J. N., Braito V., Ballo L., Gofford J., Cappi M., Mushotzky R. F., 2010b, Astrophysical Journal, 719, 700

Torrey P., et al., 2020, Monthly Notices of the Royal Astronomical Society, 497, 5292

Vogelsberger M., et al., 2014, Monthly Notices of the Royal Astronomical Society, 444, 1518

Volonteri M., 2010, The Astronomy and Astrophysics Review, 18, 279

Wang J.-M., Zhou Y.-Y., 1999, Astrophysical Journal, 516, 420

Weinberger R., et al., 2018, Monthly Notices of the Royal Astronomical Society, 479, 4056

Weinberger R., Springel V., Pakmor R., 2020, The Astrophysical Journal Supplement Series, 248, 32

Wiersma R. P. C., Schaye J., Theuns T., Dalla Vecchia C., Tornatore L., 2009, Monthly Notices of the Royal Astronomical Society, 399, 574

Yu Q., Tremaine S., 2002, Monthly Notices of the Royal Astronomical Society, 335, 965

Yuan F., Yoon D., Li Y.-P., Gan Z.-M., Ho L. C., Guo F., 2018, Astrophysical Journal, 857, 121

Zhang H., Behroozi P., Volonteri M., Silk J., Fan X., Hopkins P. F., Yang J., Aird J., 2023, Monthly Notices of the Royal Astronomical Society, 518, 2123

Zubovas K., King A., 2012, The Astrophysical Journal Letters, 745, L34

Zubovas K., Nayakshin S., King A., Wilkinson M., 2013, Monthly Notices of the Royal Astronomical Society, 433, 3079